Insights into Static Solute Strengthening and Dynamic Strain Aging Behavior of Hexagonal Close Packed Mg Alloys

---

A

Thesis

Presented to

the faculty of the School of Engineering and Applied Science

University of Virginia

---

in partial fulfillment

of the requirements for the degree

Master of Science

by

Mohammed A. Shabana

May 2022

APPROVAL SHEET

This

Thesis

is submitted in partial fulfillment of the requirements
for the degree of

Master of Science

Author: Mohammed A. Shabana

This Thesis has been read and approved by the examing committee:

Advisor: Sean Agnew

Advisor:

Committee Member: Leonid Zhigilei

Committee Member: Laurent Capolungo

Committee Member: James Burns

Committee Member: Ji Ma

Committee Member:

Committee Member:

Accepted for the School of Engineering and Applied Science:

Jennifer L. West, School of Engineering and Applied Science

May 2022

Abstract

The addition of solutes to hexagonal close packed (HCP) Mg has been extensively studied due to interests in the broad applicability of strong and lightweight alloys. However, the use of solute strengthening can pose challenges when manufacturing processes or operating conditions force the material into a range of temperatures and strain rates at which the alloys exhibit a negative strain rate sensitivity, a phenomenon which has come to be known as dynamic strain aging (DSA).

In order to develop a complete understanding of these complex phenomena, first the static (low temperature) strengthening effects of a number of important alloying additions to Mg were explored: Dy, Sc, Y, and Zn. At low temperatures, Basinski et al. postulated the principle of "stress equivalence", which stems from work on thermally activated plasticity of solid-solution-strengthened single crystal FCC and HCP alloys. Low (77 K – ambient) temperature mechanical tests of single crystals of Mg–Zn, Mg–Y, and Mg–Dy alloys were recently performed at Hokkaido University, Japan. Similarly, polycrystalline samples of Mg–Sc and Mg–Y alloys were tested at McMaster University, Canada. These data were reanalyzed within the theoretical framework of thermally activated plasticity. The analysis sought to test the applicability of the concept of "stress equivalence" outside the context of single crystal tests alone. This required the use of an effective Taylor factor acquired from a polycrystal plasticity model which accounts for the significant impacts that crystallographic texture and strain path can have on the deformation mechanism activity within Mg alloys. The results show that the principle of stress equivalence does hold, which means that predictions of the low temperature thermally activated tensile response of

textured, polycrystalline Mg alloys can be made provided the flow stress at a single strain rate and temperature is known.

At higher temperatures, the solute become mobile and the diffusional interactions between the solute and the stress fields of dislocations are held responsible for DSA and, in some cases, serrated flow. It has been widely observed that serrated flow does not ensue until reaching a critical strain, suggesting a key role of forest dislocation interactions. The second portion of this thesis seeks a deeper understanding of the role of forest dislocation interactions in DSA. Different reactions between mobile and forest dislocations can occur, including the formation of Lomer-Cottrell locks, Hirth locks, glissile junctions, and collinear annihilation. A code has been written based upon an anisotropic line tension model of dislocation interactions, which may be used to predict zero stress junction lengths as well as junction strengths (the stresses required for a mobile dislocation to escape) in the presence of solute which may bind the forest dislocation. The code has been benchmarked using theoretical predictions for FCC crystals which are available in the literature. It is now possible to extend these predictions to explore the distinctions which exist between FCC and HCP crystals since there are no locking configurations between the most common dislocations in the latter, only glissile junctions and collinear annihilation.

Keywords: Thermal Activation, Mg Alloys, Static Solute, Stress Equivalence, Dynamic Strain Aging, Line Tension Model

Acknowledgments

The first thanks, praises, and appreciations are in the name of the Entirely Merciful, the Especially Merciful.

I would like to thank Dr. Sean R. Agnew for the guidance and support that he offered during this learning experience toward the generation of this work. I am very grateful for his understanding of the problems that I have encountered in my research journey. I also give much of my deep thanks and appreciation to Dr. Jishnu J. Bhattacharyya for his huge help and contribution to important parts of this work and his patience and understanding with me in our frequent conversations about the topic of this work. I would also like to direct my thanks to Dr. Laurent Capolungo and Dr. Aritra Chakraborty (Los Alamos National Laboratory) for their great help in the second portion of the thesis work. With their help, I was able to better understand the underlying missing parameters. They provided insight and a path to approach non-trivial problem details. Also, helpful discussions with W.A. Curtin (EPFL), A. Kula (AGH University of Science and Technology), R.C. Picu (Rensselaer Polytechnic Institute), and A.E. Robertson (Georgia Institute of Technology) are gratefully acknowledged.

Lastly, I would like to thank my family and colleagues for all the encouragement, support, and helpful discussions. I would like to give my special thanks to my wife, Sally, for her understanding and patience with me as I went through this journey. Thank you for being beside me on all occasions.

Dedication

After the Absolute One, I dedicate this work to my parents and siblings. For their encouragement, their unconditional support, and their special place in my heart, I dedicate this work to my wife and grandparents. I am blessed to be part of this great family. Peace and blessings be upon you all.

Table of Contents

List of Tables

List of Figures

Abbreviations and Symbols

List of Abbreviations

2-D	***T**wo **D**imensional*
3-D	***T**hree **D**imensional*
CRSS	***C**ritical **R**esolved **S**hear **S**tress*
CS	***C**ottrell-**S**tokes*
DDD	***D**iscrete **D**islocation **D**ynamics*
DSA	***D**ynamic **S**train **A**ging*
EBSD	***E**lectron **B**ackscatter **D**iffraction*
EVPSC	***E**lasto-**V**isco**P**lastic **S**elf-**C**onsistent*
FCC	***F**ace **C**entered **C**ubic*
HCP	***H**exagonal **C**lose **P**acked*
ND	***N**ormal **D**irection*
PLC	***P**ortevin–**L**e **C**hatelier*
RD	***R**olling **D**irection*
RE	***R**are **E**arth*
SRS	***S**train **R**ate **S**ensitivity*
XRD	***X**-**R**ay **D**iffraction*
MDI	***M**obile **D**islocation **I**nstability*
FDI	***F**orest **D**islocation **I**nstability*

List of Symbols

σ	*Applied Stress*
$\dot{\varepsilon}_p$	*plastic shear strain-rate*
ρ_m	*Mobile dislocation density*
ρ_f	*Forest dislocation density*
$\vec{b}$	*Burgers vector*
$\hat{b}$	*Unit Burgers vector*
b	*Burgers vector magnitude*
$\bar{v}$	*Average dislocation velocity*
T	*Temperature*
k_B	*Boltzmann's constant*
τ	*Resolved shear stress*
ΔG	*Activation energy barrier*
ν_0	*Microscopic attempt frequency*
λ	*Effective dislocation displacement*
ΔV	*Activation volume*
$\Delta \mathrm{a}$	*Activation area*
m	*Strain rate sensitivity parameter*
$\Delta\sigma$	*Instantaneous stress change*
$\dot{\sigma}$	*Stress rate*
E_{eff}	*Effective elastic modulus*
M	*Taylor factor*

τ_{y0}	*Mechanical threshold stress*
ΔE_b	*Binding energy between solute and dislocation*
τ_y	*Shear yield strength*
C_l	*Empirical constant*
C_p	*Empirical constant*
ϕ	*Roughening exponent*
$\dot{\varepsilon}_0$	*Reference strain rate*
$\bar{\dot{\Gamma}}$	*Total accumulated shear rate*
$\dot{\gamma}^{s,g}$	*Shear rate of a given slip mode s in grain g*
w^g	*Volume fraction of grain g*
$\|\dot{\varepsilon}\|$	*Total plastic strain rate in a grain*
$\Delta\tau_s$	*Strain-rate-dependent strengthening*
$\Delta\tau_0$	*Reference stress fitting parameter*
ε_c	*Critical strain*
E	*Self-energy*
A	*Constant depending on material properties*
μ	*Shear modulus*
ν	*Poisson's ration*
α	*A dislocation's character angle*
ϕ	*Angle between junction direction and initial dislocation line*
ζ	*Angle between junction direction and a dislocation's Burgers vector*

Γ	*Length of a dislocation contour*
s	*Local position along a dislocation contour*
R/r_0	*Ratio of the outer cut-off radius to the inner cut-off radius*
W	*Dissipative work*
$u(s)$	*Displacement of segment ds*
E^p	*Potential energy*
$\dot{\gamma}_0$	*Reference shear rate*
i	*Slip mode*
n	*Stress exponent*
θ	*Individual slip system*
m^θ	*Schmid tensor*
σ^g	*Grain level stress*
τ^θ	*Current threshold stress of slip mode i*
τ_0^θ	*Initial critical resolved shear stress*
Γ^g	*Accumulated shear strain in a grain*
$\tau_0^\theta + \tau_1^\theta$	*Saturation stress*
Θ_0^θ	*Initial strain hardening rate*
σ_0	*Tensile yield strength*
c	*Solute composition*
τ^G	*Athermal stress*
τ^*	*Thermal stress*
T_1	*Temperature 1*

T_2	*Temperature 2*
ΔV_{T_1}	*Activation volume at* T_1
τ_{y,T_1}	*Yield shear strength at* T_1
τ_{y,T_2}	*Yield shear strength at* T_2
τ_{gs}	*Grain size strength*
k	*Hall-Petch parameter*
d_g	*Grain size*
$2L$	*Initial dislocation length*
Q	*Binding energy per unit length of the forest dislocation to its cluster*
x	*Length along the junction that has formed*
d	*Length along the initial forest dislocation that has escaped from its solute cluster*
$\hat{n}$	*Slip plane normal*
$\hat{x}$	*Junction unit vector*
$\hat{y}$	*Unit vector orthogonal to* $\hat{n}$ *and* $\hat{x}$
$\hat{e}$	*Unit vector orthogonal to* $\hat{n}$ *and* $\hat{b}$
a_1	*Major semiaxes of an ellipse*
a_2	*Minor semiaxis of an ellipse*
r	*Ratio between* a_1 *and* a_2
(X, Y)	*Bowed-out dislocation reference frame*
ψ	*Bow-out angle*

β	*Angle between the straight line connecting the endpoints of the bowed-out dislocation arm and the junction direction*
du	*Incremental distance displaced by the triple point toward initial crossing point*
dS_A	*Infinitesimal area swept by a dislocation in its slip plane*
X_h	*Half the length of the straight line connecting the triple point to the pinning point of the bowed-out dislocation*
E^p_{Total}	*Total potential energy*
$\tau^*_{c_m}$	*Critical stress required for a mobile dislocation to break free from a junction*
Q^*_S	*Solute saturation limit*
$\tau^*_{s_m}$	*Mobile dislocation saturation stress*
t_a	*Forest aging time*
t_w	*Average mobile dislocation waiting time*
Ω	*Characteristic strain*
mm	*Millimeters*
K	*Kelvin*
MPa	*Megapascals*
$at.\%$	*Atomic percent*

Chapter 1: Introduction

The development of durable, lightweight, fuel-efficient, and high-strength alloys has been of great interest in recent decades for many reasons including national security, economic progress and growth, and ecofriendly technological advancements. Such properties led material scientists and engineers to put a great deal of effort into the research of hexagonal-close-packed (HCP) Mg alloys. In fact, the rising interest in the application of Mg alloys has been pushed forward and encouraged by governments due to their interests and strategic foresight of the continuous global changes.

In 1993, for instance, the US federal government started what was known as the Partnership for a New Generation of Vehicles (PNGV), which largely aimed at the development of new fuel sources, powerplants, aerodynamics, and lightweight materials [1]. The main focus was to acquire technology that enabled the enhancement of fuel efficiency in automotive vehicles, reaching a goal of a three-times mileage improvement from what was common back then (jumping from 25 mpg to 80 mpg) [2,3,4]. This governmental boost in investment in a partnership between national labs, universities, and the three leading American automotive industrial companies at the time (DaimlerChrysler, Ford Motor Company, and General Motors Corporation) has led to this achievement besides other technological advances and discoveries. This partnership was then succeeded by the "FreedomCAR and Vehicle Technologies," which aimed at developing more environmentally friendly and energy-efficient highway transportation technologies assuring national security and economic benefits for the U.S. by raising its level of independence on oil exports, especially after the 1973 oil crisis [5].

Other perspectives that stand out immensely in recent years are the huge economic and environmental opportunities and prospects towards the investment in research related to Mg alloys due to the rapidly rising interest in combating climate change. Environmental scientists have been working on raising the national and international public awareness of the circumstances that the world might face due to the extreme rising levels of pollutants globally. This has led to the signing of the Paris Agreement in 2015 [6,7]. The United Nations estimates that huge opportunities are in grasp because of the 2030 plan of zero-carbon solutions implementation, which will be very competitive in energy and transportation industries.

This level of encouragement and opportunity throughout the last few decades had led material scientists and engineers to show interest in solute strengthening of Mg alloys. Research in this area has led to the observation of strain aging phenomena — in such alloys [8,9] — which pose challenges in manufacturing (metal forming) and service (e.g., crashworthiness). For example, during metal forming, orange peel patterns may be observed on surfaces (surface roughening) of Mg alloys; this is the result of localization of necking occurring under temperature and strain rate ranges in which the strain aging phenomena come into effect [10]. This imposes an economic and aesthetic design obstacle to manufacturers, as surface roughness can lead to devaluation of the material. Moreover, it is considered unsafe to operate a vehicle having components that might exhibit a reduction in strength when subjected to a range of strain rates simulating a crash [11,12].

In this thesis, the application of a static solute strengthening model on single crystal face centered cubic (FCC) and HCP alloys is extended to textured, polycrystalline Mg alloys to derive a purely experimental-parameter-based theoretical model to relate the flow stress to temperature and strain rate. Furthermore, this work seeks to show understanding and mastery of the line tension

model application to dynamic strain aging (DSA) in order to pave a path toward further research of this model for HCP Mg alloys.

Chapter 2: Background

2.1 Solid Solution Strengthening

Strengthening of alloys via addition of solutes has been of great interest, and thus has been thoroughly studied experimentally for many years. Physically, solute atoms exert a drag force (also known as solute drag) on dislocations retarding their motion; hence, a material would require a higher applied stress to allow its dislocations to overcome this solute drag in order to achieve the same level of strain [13]. Decades ago, theoreticians made nontrivial derivations relating the Critically Resolved Shear Stress (CRSS) to statistical distribution of particle obstacles to dislocation motion. The first statistical sampling model was developed in the 1960s, and it is known as the Friedel-Fleischer sampling model [14,15], which is typically used for distribute-precipitate strengthening or for alloys with high solute concentrations. This model proportionally relates the CRSS to the square root of the solute composition as shown in Figure 1.

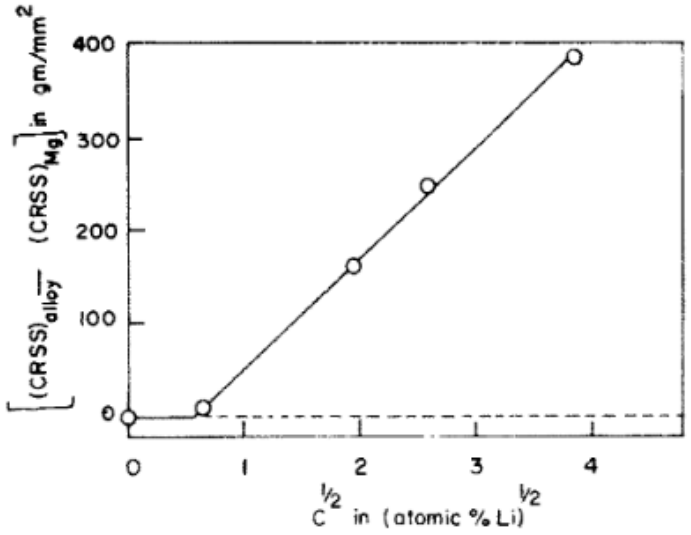

Figure 1. CRSS vs square root of different Li compositions in Mg. Open circles represent experimental data, and the solid line represents the Friedel-Fleischer sampling model [16].

About a decade later, Labusch [17,18] proposed a statistical model for the diffuse interaction between dislocations and randomly distributed solutes. This model is typically used for alloys with low solute concentrations, and it proportionally relates the CRSS to a power of 2/3 of the solute composition as shown in Figure 2.

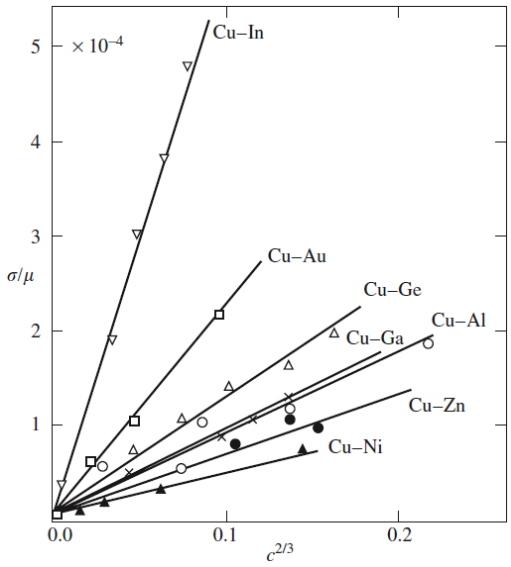

Figure 2. Yield Strength vs power of 2/3 of different solute types and compositions. Symbols represent experimental data, and the solid lines represent the Labusch sampling model [19].

Similar to the composition dependence, strength and flow stress also depend on temperature as was reported in the literature [16,19,20].

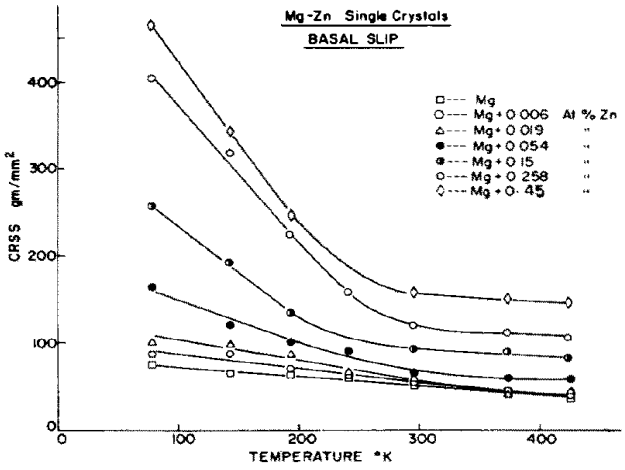

Figure 3. CRSS plot showing the dependency on both temperature and solute composition [19].

2.2 Strain Rate Sensitivity

One of the established frameworks for investigating the thermodynamics and kinetics of plasticity is to seek relationships between applied uniaxial stress (σ) and the plastic shear strain-rate ($\dot{\varepsilon}_p$). We begin with the Orowan equation

$$\dot{\varepsilon}_p = \rho_m b \bar{v} \qquad \text{Eq. 1}$$

which involves ρ_m the mobile dislocation density, b the magnitude of the Burgers vector of those dislocations, and $\bar{v}$ the average dislocation velocity. For a mobile dislocation to sweep an area, it has overcome obstacles, such as the Peierls barrier, solute atoms or forest dislocations. Thus, $\bar{v}$ is described by an Arrhenius relationship in which the activation energy barrier $\Delta G(\tau)$ is taken to be a function of the resolved shear stress (τ) on the slip plane.

$$\bar{v} = \nu_0 \lambda \exp\left(-\frac{\Delta G(\tau)}{k_B T}\right) \qquad \text{Eq. 2}$$

where ν_0 is a microscopic attempt frequency, λ is an effective dislocation displacement, k_B is the Boltzmann's constant, and T is temperature. The shape of the free energy-stress profile is often assessed in terms of the first-order Taylor series expansion,

$$\Delta G(\tau) = \Delta G^0 + \tau \frac{\partial \Delta G(\tau)}{\partial \tau} \qquad \text{Eq. 3}$$

where the slope of the free energy profile can be thought of as an activation "volume" (ΔV), which can be related to the area swept by the dislocation during an activation event by dividing by the Burgers vector $\left(\Delta a = \frac{\Delta V}{b}\right)$.

$$\Delta V = -\frac{\partial \Delta G(\tau)}{\partial \tau} \qquad \text{Eq. 4}$$

The scale of this activation volume (or area) has come to be associated with various obstacles that may control the relationship between applied stress and strain rate. Experimentalists assess this activation volume using either strain rate jump (e.g., Figure 4) or stress relaxation tests.

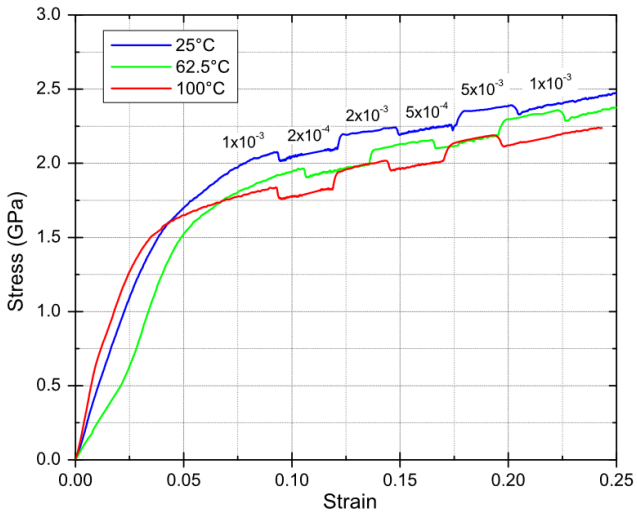

Figure 4. Strain rate jump tests for nanocrystalline nickel at different temperatures [21].

The strain rate jump test permits assessment of the steady state Strain Rate Sensitivity (SRS) parameter (also denoted m) through the measured instantaneous stress change ($\Delta\sigma$) between two different strain rates using the methodology described by Basinski [22] and Wagoner [23], which is briefly illustrated in Figure 5. This is possible due to the fact that m is expressed in the form of

$$m = \frac{\partial \ln \sigma}{\partial \ln \dot{\varepsilon}_p} = \frac{\Delta\sigma}{\sigma \Delta \ln \dot{\varepsilon}_p} \qquad \text{Eq. 5}$$

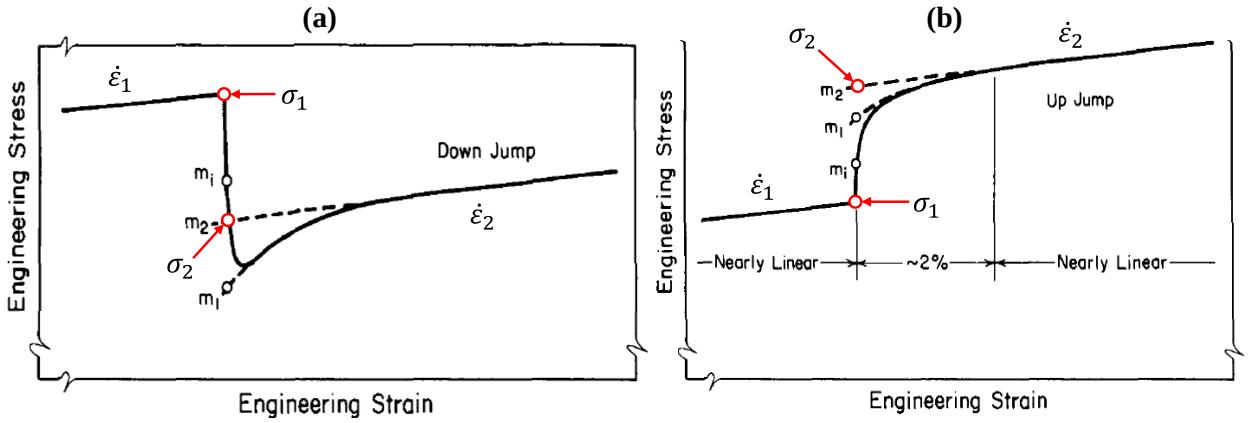

Figure 5. Wagoner's approach to determine the stress change from a strain rate (a) down jump and (b) up jump from a strain rate jump test.

In the case of stress relaxation testing, the SRS can still be determined since the plastic strain rate during stress relaxation is equivalent to the negative ratio between the time derivative of the stress ($\dot{\sigma}$) and the effective elastic modulus (E_{eff}) of the sample and machine, $\dot{\varepsilon}_p = -\dot{\sigma}/E_{eff}$. As described by Caillard and Martin [24], the stress rate can be obtained by fitting the recorded stress change with time with a logarithmic function and then taking the time derivative of the fitted expression. In either case, differentiating Eq. 1 to obtain the SRS and simplifying the resulting differential leads to

$$\frac{\partial \ln \dot{\varepsilon}_p}{\partial \ln \tau} = -\frac{\tau}{k_B T}\frac{\partial \Delta G(\tau)}{\partial \tau} = \frac{\tau \Delta V}{k_B T} \qquad \text{Eq. 6}$$

If one performs experiments on single crystals, the relationship between the applied stress state and the resolved shear stress (τ) on the active slip plane is readily obtained through the Schmid law. For polycrystalline cubic metals, it has frequently been adequate to assume conditions of "polyslip" within each of the grains during macroscopic plasticity, and hence, τ is reasonably related to σ by the upper bound approximation, the Taylor factor (M) by $\sigma = M\tau$. Under these conditions, the relationship between the rate sensitivity and the activation volume may be simply expressed as

$$\Delta V = \frac{M k_B T}{\sigma m} \qquad \text{Eq. 7}$$

and the Haasen plot representation of this relation simply obtained by substituting Eq. 5 into the inverse of Eq. 7 as

$$\frac{1}{\Delta V} = \frac{\Delta \sigma}{M k_B T \Delta \ln \dot{\varepsilon}_p} \qquad \text{Eq. 8}$$

2.3 Haasen Plots

A plot of the inverse activation volume as a function of the flow stress is called a "Haasen plot" in the literature. This plot is developed on the premise of the Cottrell-Stokes (CS) law, which states that the CS ratio of flow stresses of a material at two different temperatures, for a specified

strain rate, does not depend on the level of strain-hardening [25]. Peter Haasen [26] mentioned that the CS law would still be valid with additional contribution to the flow stress and determined that a difference between flow stresses (instead of the CS ratio) would present a linear relationship with flow stress. Since a change in temperature leads to changes in the elastic modulus and the dislocation core configuration, an analogous understanding of the CS Law was developed by employing a strain rate change at a specified temperature instead of a temperature change at a specified strain rate [27]. This change in flow stress with respect to a change in strain rate corresponds to the definition of SRS. Thus, the stress change and the SRS can be related to the inverse of the activation volume by Eq. 8.

For this type of plot, the abscissa represents the flow stress, and the ordinate represents the inverse of the activation volume. Other than the data themselves, the important features in a Haasen plot are the slope (i.e., SRS) and the intercept (i.e., activation volume at yield); a negative slope suggests undergoing DSA. As per Kocks and Chen [28], if the intercept is positive, the dominating obstacles are more thermal than dislocations (e.g., solutes); on the other hand, the dominating obstacles are more athermal than dislocations (e.g., grain boundaries and large, unshearable particles), if the intercept is negative. As discussed by the definition and setup of the Haasen plot, the data — and thus, the SRS and activation volume at yield — depend on the temperature and strain rate conditions, as illustrated in Figure 1(a) and Figure 1(b), respectively [29].

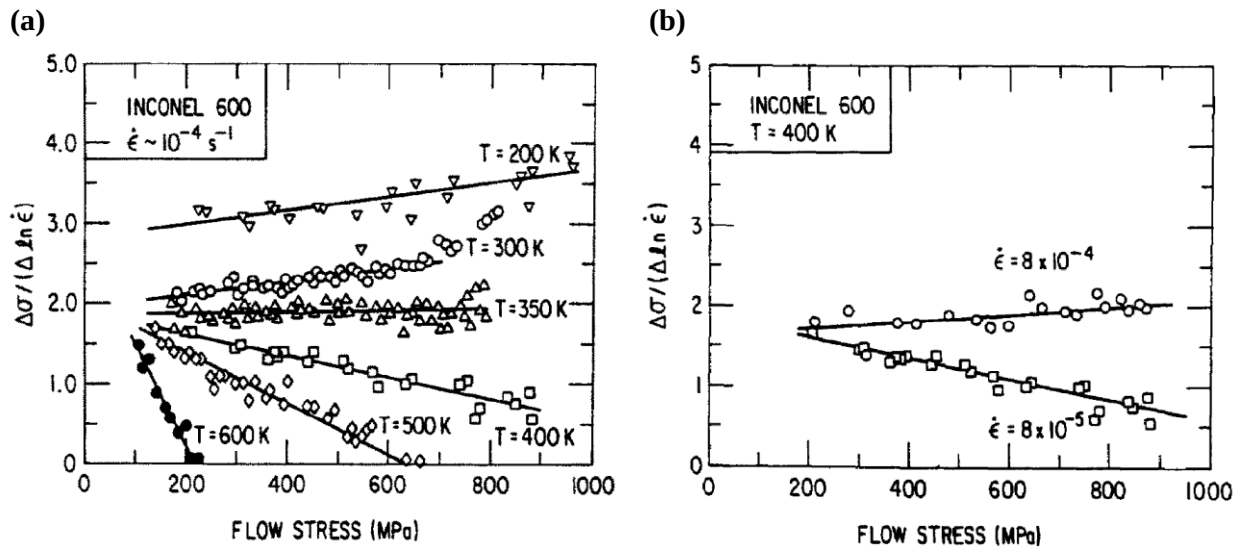

Figure 6. Haasen plots of INCONEL 600 generated from rate jump test (a) at the same strain rate but at different temperatures, and (b) at the same temperature but at different strain rates.

2.4 The Principle of Stress Equivalence

In 1972, Basinski et al. [30] performed tests on Cu-based alloy single crystals and extracted data from the literature for Ag- and Mg-based alloys tested at 78 and 200 K. They used the yield stress change between the two temperatures as an assessment of thermal activation and plotted the results against the corresponding yield strengths at 78 K, as illustrated in Figure 7 and Figure 8. From these results, they deduced the principle of "stress equivalence," which states that solid solution alloys of a given base element have the same activation volume if they have the same yield strength at a given temperature and strain rate, independent of the solute atoms involved and their concentrations.

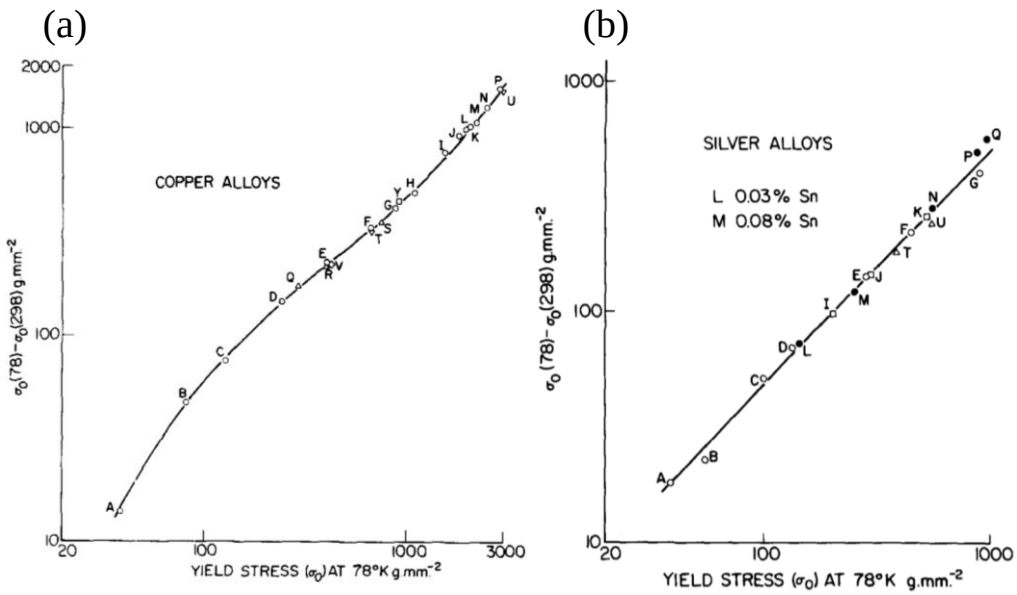

Figure 7. Temperature dependent yield plot for single crystal FCC (a) Cu and (b) Ag alloys.

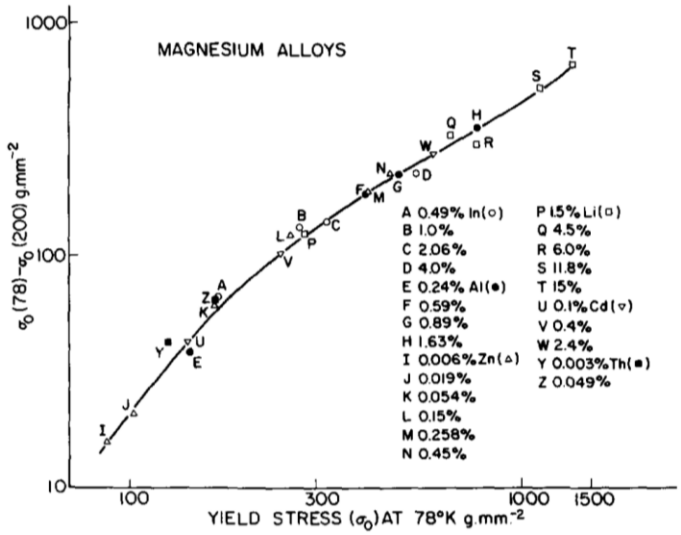

Figure 8. Temperature dependent yield plot for single crystal HCP Mg alloys.

2.5 Previous Modelling work on solid solution strengthening

In a study of thermal activation by Nabarro [31], he derived a model for activation volume dependency on flow stress and directed attention to the "stress equivalence" principle by noting that his model might help explain the observations of Basinski et al. [30]. His model depends largely on the work of Labusch [32,33], who proposed his statistical solute distribution model — as discussed in Section 2.1 — in the same year that Basinski et al. introduced stress equivalence. In a related work, Nabarro [34] used this model to predict the solute compositional limit above which the Labusch statistical sampling model is valid. He derived a parameter that defines the transition between this model and the Friedel-Fleischer sampling model. Indeed, he revealed that the compositional limit is very small when compared to the nominal solute compositions in metallic alloys, and thus, the Labusch model is valid in the vast majority of cases of practical interest. The details of the chronological development are nicely articulated by Argon [19].

Leyson and Curtin [35,36] recently introduced a model which builds upon this foundation and makes use of binding energies, ΔE_b, between solute and dislocations which are obtained from atomistic simulation. The complete model admits that dislocations may overcome these barriers by bow-outs of various sizes, depending upon the thermal energy available (i.e., the temperature). The following expressions have been shown to well describe the flow stress within the corresponding high, intermediate, and low stress regimes (relative to the mechanical threshold stress, τ_{y0}):

$$\frac{\tau_y(T)}{\tau_{y0}} = \begin{cases} 1 - \left(\frac{k_B T}{\Delta E_b} \ln\left(\frac{\dot{\varepsilon}_0}{\dot{\varepsilon}}\right)\right)^{\frac{2}{3}}; & \frac{\tau_y(T)}{\tau_{y0}} > 0.5 \\ \exp\left(-\frac{k_B T}{C_l \Delta E_b} \ln\left(\frac{\dot{\varepsilon}_0}{\dot{\varepsilon}}\right)\right); & 0.2 < \frac{\tau_y(T)}{\tau_{y0}} < 0.5 \\ \left(\frac{1}{C_p}\frac{k_B T}{\Delta E_b} \ln\left(\frac{\dot{\varepsilon}_0}{\dot{\varepsilon}}\right)\right)^{-\frac{1}{\phi}}; & \frac{\tau_y(T)}{\tau_{y0}} < 0.03 \end{cases} \quad \text{Eq. 9}$$

where k_B is Boltzmann's constant, T is the temperature, $\dot{\varepsilon}_0$ (~ 10^4 s^{-1}) is the reference strain rate, $\dot{\varepsilon}$ is applied strain rate, and ϕ is a roughening exponent. C_l and C_p are empirical constants within the corresponding logarithmic (intermediate stress) and power law (low stress) regimes. Only the latter regime is of present interest, and the constant C_l ~0.55 fits the predictions of the full theory.

The corresponding activation volumes, used to describe the stress dependence of the activation free energy, as in Eq. 4, are given as:

$$\Delta V(\tau_y, T) = \begin{cases} \frac{3}{2}\frac{\Delta E_b}{\tau_{y0}}\left(\frac{k_B T}{\Delta E_b} \ln\left(\frac{\dot{\varepsilon}_0}{\dot{\varepsilon}}\right)\right)^{\frac{1}{3}}; & \frac{\tau_y(T)}{\tau_{y0}} > 0.5 \\ C_l \Delta E_b \tau_y^{-1}; & 0.2 < \frac{\tau_y(T)}{\tau_{y0}} < 0.5 \\ \left(\phi k_B T \ln\left(\frac{\dot{\varepsilon}_0}{\dot{\varepsilon}}\right)\right)\tau_y^{-1}; & \frac{\tau_y(T)}{\tau_{y0}} < 0.03 \end{cases} \quad \text{Eq. 10}$$

The applicability of this model was demonstrated for FCC metals such as Al-Mg [37] alloys as well as HCP metals such as Mg-Al alloy single crystals oriented for basal slip [38]. Tehranchi et al. [39] used this model on Mg-Al and Mg-Zn alloys to predict the basal plane CRSS at different temperatures and compositions; they verified their predictions with experimental data from the literature [16,68] (Figure 9).

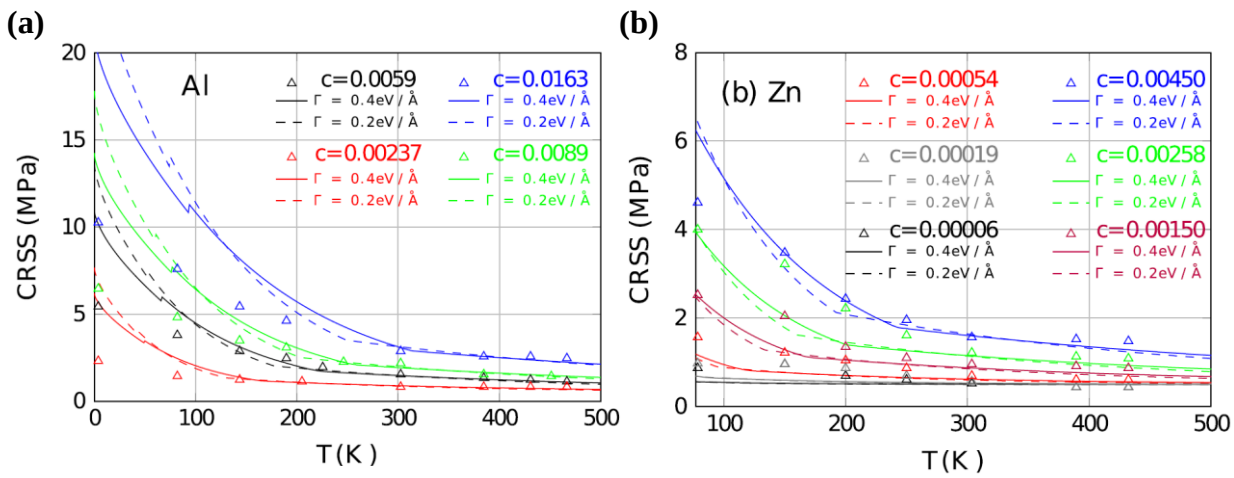

Figure 9. Dependence of CRSS on temperature for different compositions of (a) Al and (b) Zn in binary Mg alloys. The open triangles represent experimental data [16,68]. The solid and dashed lines represent predictions using the Leyson-Curtin Model for two different line tension values.

2.6 Polycrystal Plasticity Modelling

In non-cubic metals like Mg and its alloys, multiple deformation modes can be potentially active, and the relative activities of these modes influence the aggregate response. Thus, the macro (polycrystal) -to- micro (slip system level) conversion is not as straightforward as it is in the case of FCC metals, where a single Taylor factor is generally sufficient to connect the measurements of random polycrystals to the resolved shear quantities of interest [40]. Crystal plasticity simulations provide a means of quantifying the strain accommodated by these different modes and this enables one to compute an *effective* Taylor factor (*M)* connecting the shear quantities at the grain level to those measured at the polycrystal/macroscopic level for a given texture and strain path. This Taylor factor can be defined as the volume weighted ratio of the total accumulated shear rate $\bar{\dot{\Gamma}}$ to the norm of the total plastic strain rate in a grain $\|\dot{\varepsilon}\|$, modified for uniaxial case [41]:

$$M = \frac{\bar{\dot{\Gamma}}}{\|\dot{\varepsilon}\|} = \frac{\sqrt{\frac{3}{2}}\sum_g \sum_s \dot{\gamma}^{s,g} w^g}{\left\|\dot{\varepsilon}_p^g\right\|} \qquad \text{Eq. 11}$$

where $\dot{\gamma}^{s,g}$ is the shear rate of a given slip mode s in a given grain g, and w^g is the volume fraction of the corresponding grain.

With this background, the principle of stress equivalence is further evaluated with data from the literature for single crystal Mg alloys (including recently published data from Mg-Zn, Mg-Y, and Mg-Dy [42]) as well as data from polycrystalline Mg-rare earth (RE) element alloys (Mg-Sc and Mg-Y) [76,78]. A rational methodology, accounting for grain size effects and the Taylor factor, is presented for comparing data obtained from polycrystals and single crystals.

2.7 Strain Aging

Experimentally, if a sample is loaded until some point {a} (Figure 10) of plastic deformation, then it was unloaded from that point and immediately reloaded, the stress-strain curve would follow the initial path of the curve. However, if the unloaded sample was allowed to strain age (i.e., no immediate reload after unload from point {a}), the stress-strain curve would not follow the initial path; rather, a new yield peak pint would develop at point {a'}.

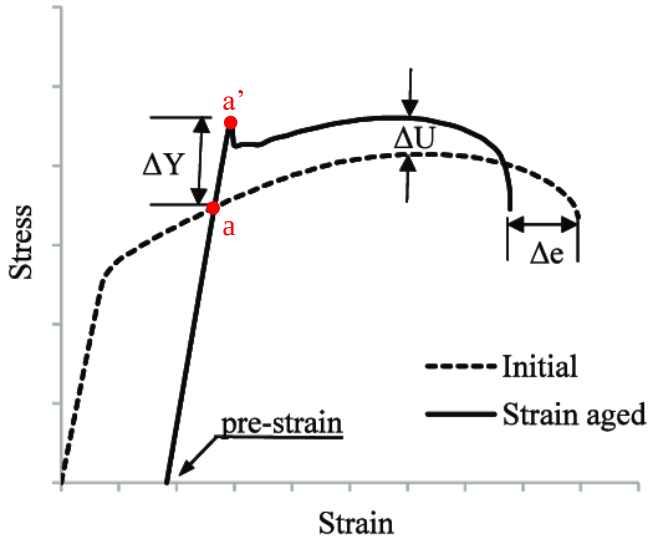

Figure 10. Schematic showing the difference observed in a stress-strain curve between the cases of presence and absence of strain aging [43].

This phenomenon can be explained such that when the temperature gets high enough, the solute can diffuse toward the dislocation core as was discussed in the literature by Cottrell and Bilby [44], creating a region of solute — surrounding the dislocation core — called the Cottrell atmosphere (Figure 11). The formation of this atmosphere has an additional impact on the pinning of dislocations, and thus can result in the observable macroscopic behavior of yield point peaks and formation of Lüders bands [45], which is a manifestation of strain aging.

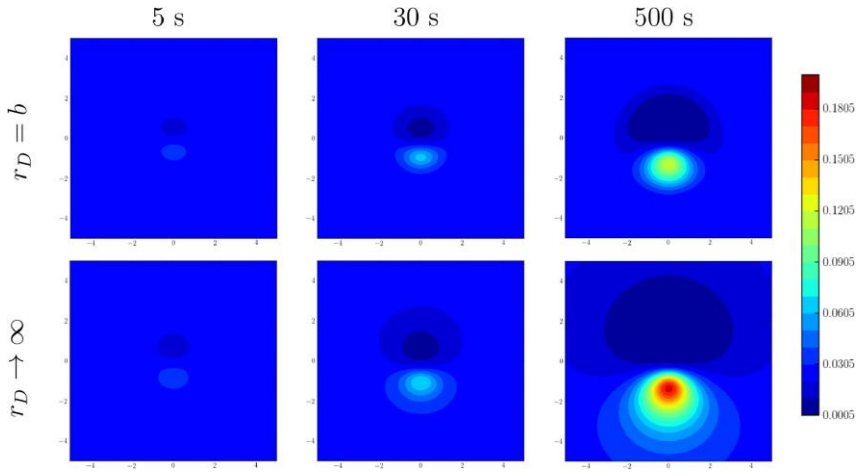

Figure 11. Simulated formation of the Cottrell (solute) atmosphere in an Al-Mg alloy [46].

2.8 Dynamic Strain Aging

As mentioned in Section 2.7, Strain aging is a solute-induced effect whereby solute atmospheres form around dislocations, thereby immobilizing the dislocations until the stress reaches a sufficiently high level to cause them to “break away” from the solute. It can give rise to effects such as yield point peaks. Because it requires solute to diffuse to the core of dislocations in order for this effect to occur, it has both time- and temperature-dependences. Dynamic strain aging (DSA) occurs when the temperature is sufficiently high and/or the strain rate is sufficiently low that the solute can repeatedly capture the dislocations, and the material exhibits a negative SRS, a defining characteristic of DSA. Within a range of temperatures and strain rates, this phenomenon might cause repeated pinning and unpinning of dislocations from moving obstacles (in this case, solute atmospheres), giving rise to the Portevin–Le Chatelier effect (PLC) (i.e., serrated or jerky flow). Figure 12 illustrates the relationship between the SRS and the appearance of DSA and PLC within a range of temperatures and strain rates [29].

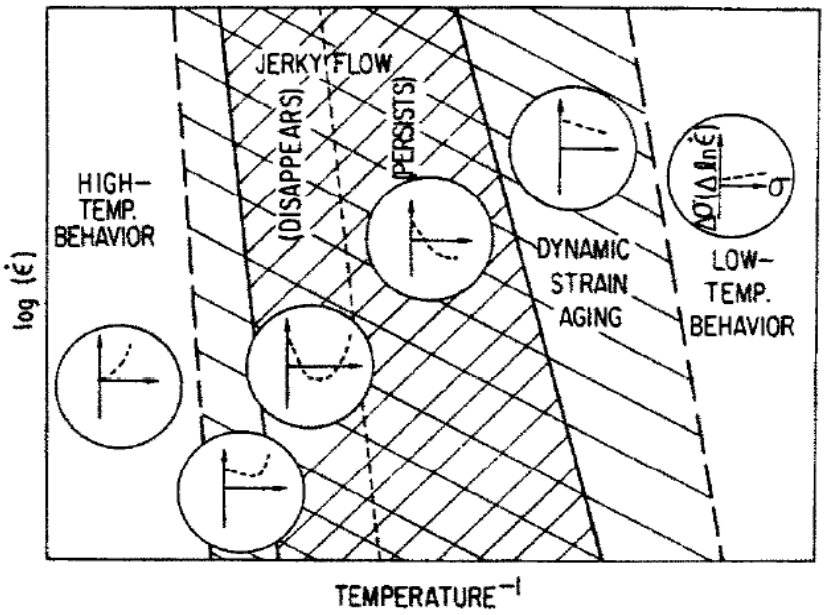

Figure 12. A schematic showing the appearance of DSA and PLC (jerky flow) as well as the shape of the Haasen plot slope (i.e., SRS) shown within the small inset plots within the circles representative of different temperature and strain rate ranges.

Placing DSA in a more general framework, there are many studies in the literature that deal with these phenomena and report other possible mechanisms that may be responsible for them. For instance, some materials can undergo stress-induced phase transformation which can lead to the observance of negative SRS [47]. Other studies have shown that precipitates also play a role in DSA and that precipitate types (i.e., shearable and nonshearable particles) can have different impacts on serrations [48,49]. Furthermore, Chun and Davies reported that texture of Mg alloys is very important because the SRS is affected by the relative activity of twinning, which can lead to negative SRS [50]. All these different mechanisms can contribute to DSA; however, the current work focuses on the contribution of solute and, as will be described in detail below, their possible effects on dislocation junction formation.

Phenomenological DSA models have been developed, but it was shown by Curtin et al. [51] that the parameters employed in these models were not realistic because they did not account

for details, such as the possibility of "cross-core solute diffusion," which states that solute atoms jump directly across the slip plane, from the compressive to the tensile side, in the dislocation core. To illustrate, the strain-rate-dependent strengthening ($\Delta\tau_s$) model that Curtin refers to takes the form

$$\Delta\tau_s(\dot{\varepsilon}_p) = \Delta\tau_0\left(1 - \exp\left(-\frac{\dot{\varepsilon}_0}{\dot{\varepsilon}_p}\right)^{\frac{2}{3}}\right) \quad \text{Eq. 12}$$

where $\Delta\tau_0$ is the reference stress fitting parameter. The approaches using this model neglecting "cross-core solute diffusion" suffer from a fundamental problem because they use vacancy-assisted diffusion $\dot{\varepsilon}_0$ values that are approximately six orders of magnitude less than experimentally $\dot{\varepsilon}_0$ derived values ($\sim 10^{-4}$). Accounting for the mechanism of pipe diffusion along the dislocation core [52] does not fix this issue.

Besides the theory of "cross-core" diffusion, the role of "forest dislocations," which serve as additional obstacles to mobile dislocations has been emphasized [53,54] because DSA phenomena often do not occur until reaching a critical strain ε_c [55,56] as shown in Figure 13. Therefore, it is important to consider possible interactions between mobile and forest dislocations in light of their role in the occurrence of DSA.

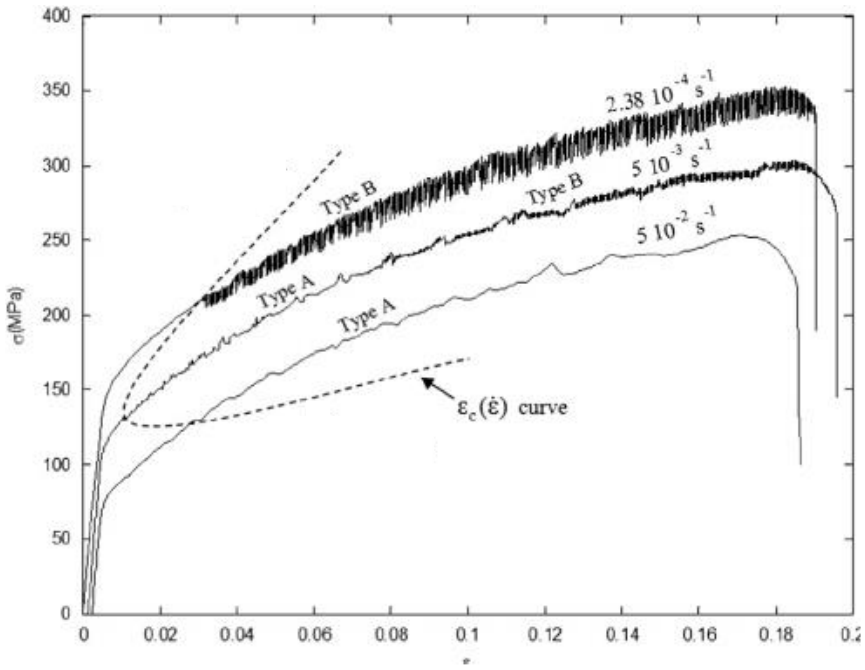

Figure 13. Room temperature stress-strain curve of Al-3.2%Mg alloy at different strain rates showing the critical strain that is reached before the beginning of the jerky flow.

2.9 Anisotropic Dislocation Line Tension Model

Bacon et al. [57] developed a dislocation line tension model taking into account the anisotropy of a dislocation. This model sets the self-energy (E) of a dislocation as

$$E(\alpha) = \int_{\Gamma} A(1 - \nu \cos^2(\alpha))\, ds \qquad \text{Eq. 13}$$

where ν is the Poisson's ratio, α is the dislocation character angle, Γ is length of the dislocation contour, s is a local position along Γ, and A is a constant — depending on the material properties — defined as

$$A = \frac{\mu b^2}{4\pi(1-\nu)} \ln\left(\frac{R}{r_0}\right) \quad \text{Eq. 14}$$

where μ is the shear modulus, b is the Burgers vector, and R/r_0 is the ratio of the outer cut-off radius to the inner cut-off radius. Note that, per Eq. 13, ignoring ν (setting $\nu = 0$) leads to cancelling out the contribution of the dislocation character from the self-energy (i.e., removing the effect of the dislocation directionality).

Under some applied resolved shear stress τ, a dislocation can bow out or sweep some area in the slip plane. This is equivalent to undergoing plasticity, which is a dissipative process. Therefore, the dissipative work done to sweep an area in the slip plane must be integrated over the path taken from the initial state to the final one by the following equation

$$W = \int_{\Gamma} \tau b u(s)\, ds \quad \text{Eq. 15}$$

where $u(s)$ is the displacement of segment ds. Now, the potential energy is simply

$$E^p = E - W \quad \text{Eq. 16}$$

Many scientists utilized this model in their investigations of dislocation-dislocation interactions [58,59]. Dupuy and Fivel [60] investigated the effect of initial dislocation configurations in FCC crystals on the extent of different dislocation junction types, such as those listed in Table 1. Note that their study did not include collinear annihilation, which means that two dislocations with opposite vectors ultimately annihilate when they encounter each other; however,

it is included in the table because it is a possible dislocation-dislocation interaction that is often observed [61].

Table 1. Example cases of dislocation-dislocation interactions in FCC crystal structures resulting in different junction formations.

Type	**Interaction**	**Junction Direction**	**Junction Slip Plane**	**Description**
Hirth Lock	$\frac{1}{2}[0\bar{1}1]+\frac{1}{2}[011]\rightarrow[001]$	$(111)\times(1\bar{1}1)\rightarrow[10\bar{1}]$	(010)	Junction does not lie in a favorable slip plane
Lomer Lock	$\frac{1}{2}[\bar{1}10]+\frac{1}{2}[101]\rightarrow\frac{1}{2}[011]$	$(111)\times(\bar{1}11)\rightarrow\ [0\bar{1}1]$	(100)	Junction does not lie in a favorable slip plane
Glissile Junction	$\frac{1}{2}[\bar{1}10]+\frac{1}{2}[0\bar{1}1]\rightarrow[\bar{1}01]$	$(111)\times(\bar{1}11)\rightarrow\ [0\bar{1}1]$	(111)	Junction lies in a favorable slip plane
Collinear Annihilation	$\frac{1}{2}[0\bar{1}1]+\frac{1}{2}[01\bar{1}]\rightarrow[000]$ $\vec{b}+(-\vec{b})\rightarrow\vec{0}$	—	—	No junction formation

In their investigation Dupuy and Fivel used symmetric dislocation configurations (i.e., both the mobile and forest dislocations started with similar ϕ angles between the dislocation arm and the junction direction) and determined the normalized junction length using a force equilibrium of the anisotropic dislocation line tension model (Figure 14).

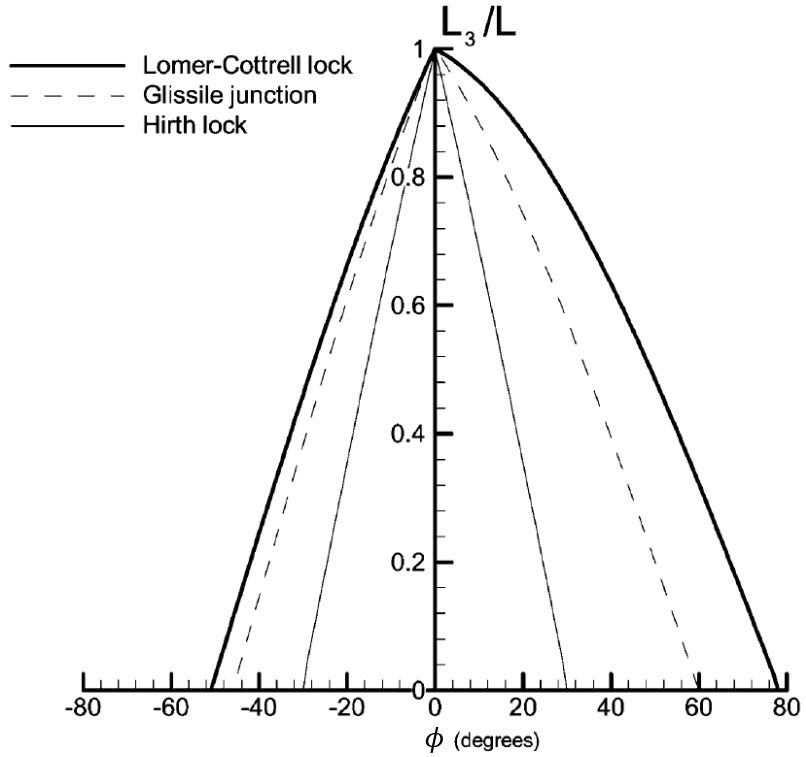

Figure 14. The dependency of different junction formations on the initial configuration of symmetric interacting dislocations determined using the anisotropic dislocation line tension model.

What is interesting about this model is that other studies implemented more complicated models involving the use of nodal [59,62] and atomistic simulations [63,64,65], and they it was shown that the results of the simple anisotropic line tension model are in very good agreement with the more complicated approaches. Figure 15 represents the normalized Lomer-Cottrell lock length using the isotropic (i.e., not accounting for the effect of dislocation directionality by ignoring the Poisson's ratio — i.e., $\nu = 0$) and anisotropic line tension models and a nodal model. The isotropic line tension model was used in 1960 by Saada [66] to tackle the same problem, but it was found later that the anisotropic model is in better agreement with other more sophisticated models as shown in Figure 15.

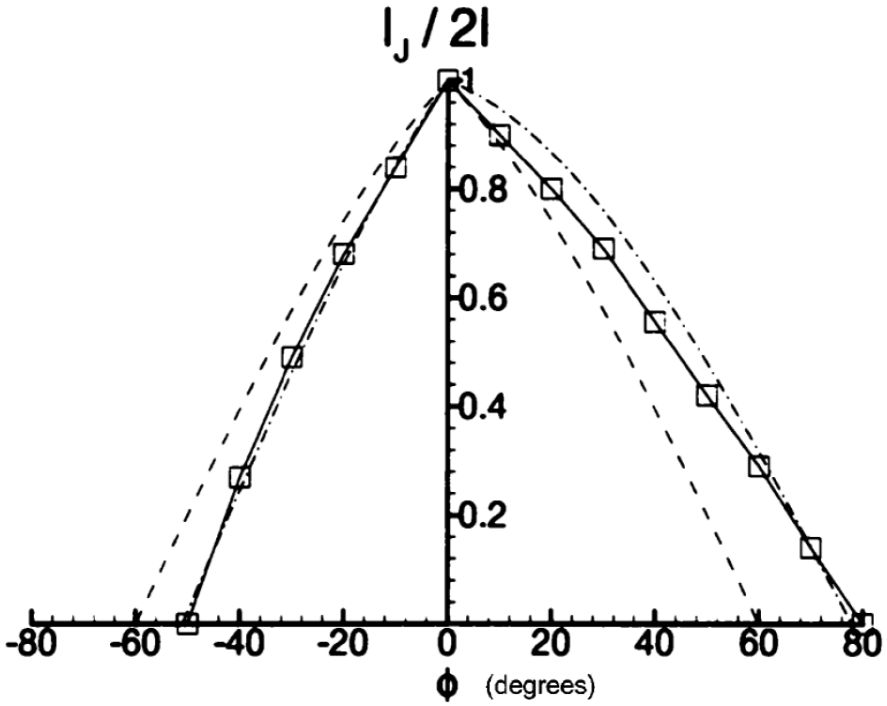

Figure 15. Lomer-Cottrell lock formation. The dashed and dash-dotted lines represent the isotropic and anisotropic line tension models, respectively. The streaked squares represent results from nodal model simulations [62].

Chapter 3: Part I – Effects of Static Solute on Thermally Activated Dislocation Motion

The work in this chapter has been previously published in the journal of *Materials Science and Engineering: A* in 2021 [67]. As the lead author, I performed the investigation and data analysis mentioned in this chapter on experimental data that were provided by one of the contributing authors. I have also performed the writing, reviewing, and editing of the work. The following list represents the contributing authors and their role in this study:

I. Dr. Jishnu J. Bhattacharyya (University of Virginia, VA, USA) helped in the investigation, performed the polycrystal plasticity modelling, and helped in writing, reviewing, and editing the paper.

II. Dr. Marek Niewczas (McMaster University, Hamilton, ON, Canada) provided the experimental data upon which the investigation is based, reviewed, and edited the paper.

III. Dr. Sean R. Agnew (University of Virginia, VA, USA) provided help and insight in the investigation, provided guidance on the conceptualization of the problem and analysis, and helped in the writing, reviewing, and editing of the paper.

The Mg alloying elements considered by Basinski et al. [30] included commonly employed Al and Zn [68] along with elements of scientific interest like Cd [69], In [68], Li [70] and Th [71]. In recent times, there has been great interest in alloys of rare earth elements, such as Sc [72,73,74] and Y [75]. Making single crystals from alloys with very limited solubility like Sc is challenging, making it of interest to determine what can be learned about fundamental mechanisms from the study of polycrystals.

3.1 Experiments

The present work examines the thermal activated constitutive response of polycrystalline Mg-Sc and Mg-Y binary alloys. The experimental details have been published elsewhere [76,77,78,79], hence is not repeated here. Only a brief description is provided for the benefit of the reader.

Mg-Sc [76,77] and Mg-Y [78,79] alloys were cast as cylindrical ingots in an Ar environment at a pour temperature ~ 760°C. The ingots were then homogenized under Ar atmosphere at 520°C for 12 - 24 hours and then annealed at ~460°C in air for 20 – 60 minutes before applying the rolling procedure (hot-rolling for Mg-Sc and cold-rolling for Mg-Y) to get the final desired sheet thickness (3 mm). Tensile specimens with loading axis parallel to the rolling direction (RD) were extracted from these rolled sheets. Finally, the Mg-Sc samples were annealed in air at 420°C for 20 minutes while Mg-Y samples were annealed in air at 500°C for 15 minutes in order to recrystallize and relieve internal stress caused from processing.

The textures of all the samples were measured by XRD and/or EBSD, revealing a typical basal texture with peak intensity between 4 and 6 multiples of random distribution parallel to the sheet normal direction (ND) intensity in the basal pole figure [76,78]. The lineal intercept grain

sizes of the samples were determined by conventional optical metallography and found to lie between 50 and 200 μm, [76,78] with precise values discussed below.

Monotonic tensile tests were performed on the binary alloys samples at 78 and 298 K using a constant crosshead velocity corresponding to an initial strain rate of 2.8×10^{-4} s^{-1} [76,78]. The details of the experimental set-up are provided in [77,79]. In all cases, the 0.2% offset stress is used as the yield stress. Strain rate jump tests between 2.8×10^{-4} s^{-1} and 2.8×10^{-5} s^{-1} were used to construct Haasen plots [76]. The strain between the strain rate jumps was sufficient to eliminate the transients resulting from machine inertia and attain a steady-state flow. Both up-jump and down-jump tests were performed, and the results were essentially identical [76]. Following the procedure outlined by Basinski et al. [80] and Wagoner [81], back extrapolation of the steady-state stress to the strain at which the rate jump was carried out, was used for computing the change in flow stress due to a strain rate change.

3.2 Polycrystal Plasticity Modelling

Among several polycrystal plasticity homogenization schemes, the Elasto-ViscoPlastic Self-Consistent (EVPSC) strategy proposed by Molinari et al. [82,83] and detailed elsewhere [84,85,86] has been shown to be adequate in describing the constitutive response of non-cubic (including Mg) alloys, including flow curves, texture evolution, plastic strain anisotropy (r-values) and relative slip activities for various strain paths [87,88,89,90]. In brief, the polycrystal is represented in the model as a collection of crystal orientations with volume fractions determined by the experimentally measured initial texture. The appropriate macroscopic boundary conditions (e.g., for the present case, uniaxial tension, strain-rate jump, stress relaxation, along the RD) are

imposed on the polycrystal and the grains respond according to a specified constitutive rule. In this model, the viscoplastic response is typically approximated by a power law flow rule over a specific temperature and strain rate regime of interest: $\dot{\varepsilon}_p = \dot{\gamma}_0 \sum_i m^\theta \left(\frac{m^\theta : \sigma^g}{\tau^\theta}\right)^n$ where, $\dot{\gamma}_0$ is the reference shear rate, m^θ is the Schmid tensor, σ^g is the grain level stress and τ^θ is the current threshold stress of slip mode *i*, and *n* is the stress exponent. The strength τ^θ of an individual slip system, θ, is given by an initial critical resolved shear stress (CRSS), τ_0^θ which then evolves according to the Voce strain hardening rule: $\frac{\partial \tau^\theta}{\partial \Gamma^g} = \Theta_0^\theta \left(1 - \left(\frac{\tau^\theta - \tau_0^\theta}{\tau_1^\theta}\right)\right)$ where $\Gamma^g = \sum_\theta \gamma^\theta$, the accumulated shear strain in a grain, $\tau_0^\theta + \tau_1^\theta$ is the saturation stress, and $\Theta_0^\theta$is the initial strain hardening rate. Thus, there are three fitting parameters for each slip mode.

For the present modeling work, the stress exponents reported by Wang et al. [84] for Mg alloy AZ31B are used for the purpose of illustration (i.e., the *n* value for basal, prismatic, <c+a> slip and extension twinning are 100, 80, 33 and 120, respectively). The model was used to simulate strain rate jump tests as well as stress relaxation tests along the rolling direction (RD) of a moderately basal-textured Mg polycrystal sheet. The texture employed for these simulations has a maximum strength of ~4 m.r.d, typical of the rolled Mg-Sc and Mg-Y alloys examined in the present work.

Our previous publications on Mg alloys have focused on relating the CRSS values to the relevant strengthening mechanisms e.g., lattice resistance, Hall-Petch effect, solid solution, precipitation as well as forest strengthening [91,86,92,93,94]. In the present work, a different approach is taken. Here, we did not attempt to fit each individual experimental flow curves. Rather we have examined the holistic behavior of the general class of materials under consideration, under

the relevant strain path (i.e., RD tension). Hence, the simulations were carried out using CRSS values and Voce hardening parameters that are typical of Mg alloys e.g., where the ratios of the CRSS values for basal, prismatic, 2^{nd} -order <c+a> slip and extension twinning are 1:5:8:2, respectively.

Simulations of monotonic tensile tests were used to explore the relative activities of slip and twinning modes, especially through the elastoplastic transition (yielding) as well as to determine an effective Taylor factor using Eq. 11, for the subsequent activation analysis. Since strain rate jump tests were employed to determine the activation volumes experimentally, simulations of the same were carried out by abruptly changing the imposed strain rate to a value either greater than (up-jump) or lower than (down-jump) the initially imposed strain rate, in order to determine if there was a radical change in the mode activity during the rate jumps. Similarly, simulations of repeated stress relaxation test were also simulated since some researchers have advocated for the use of this approach to determine *true* activation volumes. First, the sample is subjected to uniaxial tension along RD up to a specified strain level. Then the total strain (along RD) is held constant for a certain duration (e.g., 30s). After the prescribed duration of relaxation, the uniaxial boundary conditions are enforced again until the stress level reaches the value at which the first relaxation was carried out (within 5 MPa), following which the relaxation condition is imposed again. This process was repeated three times to simulate the repeated stress relaxation test.

3.3 Results

3.3.1 Constitutive response

Figure 16 shows the flow curves for uniaxial tension along RD at 78 K for both the alloys, Mg-Y and Mg-Sc. It can be observed from Figure 16(a) that the yield strength increases notably with increasing Y compositions. The yield strengths for the three Mg-Sc compositions in this study show a slight variation of about 20 to 30 MPa as seen in Figure 16(b).

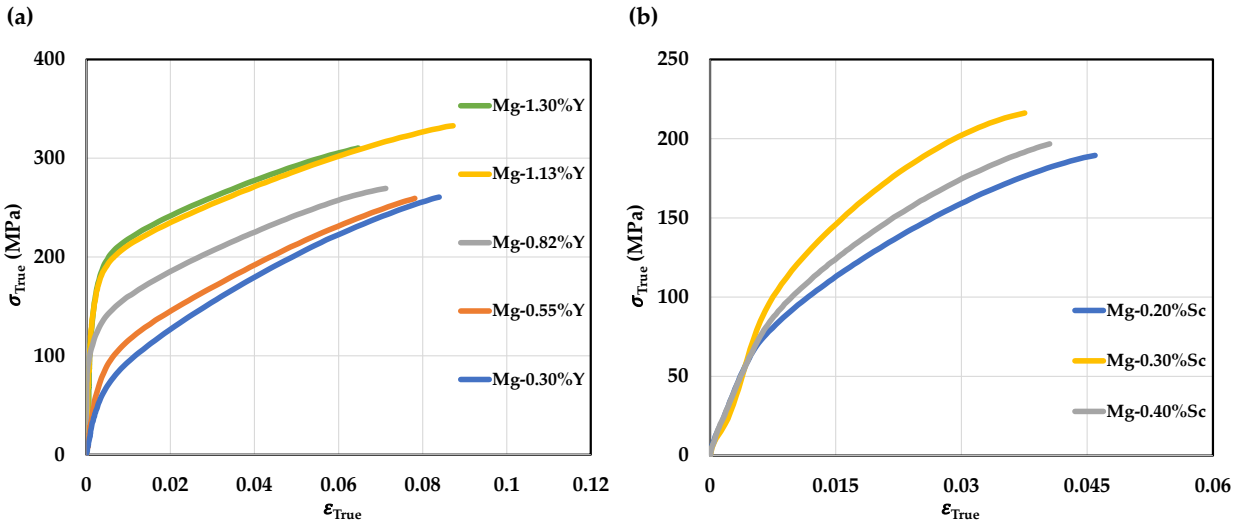

Figure 16. Stress-Strain curves for uniaxial tensile tests for different compositions of Mg-Y and Mg-Sc alloys at 78 K reproduced from Refs. [23,25].

3.3.2 Polycrystal Plasticity Modelling

Figure 17 shows the results of typical EVPSC simulations of monotonic tensile tests performed on virtual samples with textures which are similar to those of the Mg-rare earth element alloys examined experimentally in the present study.

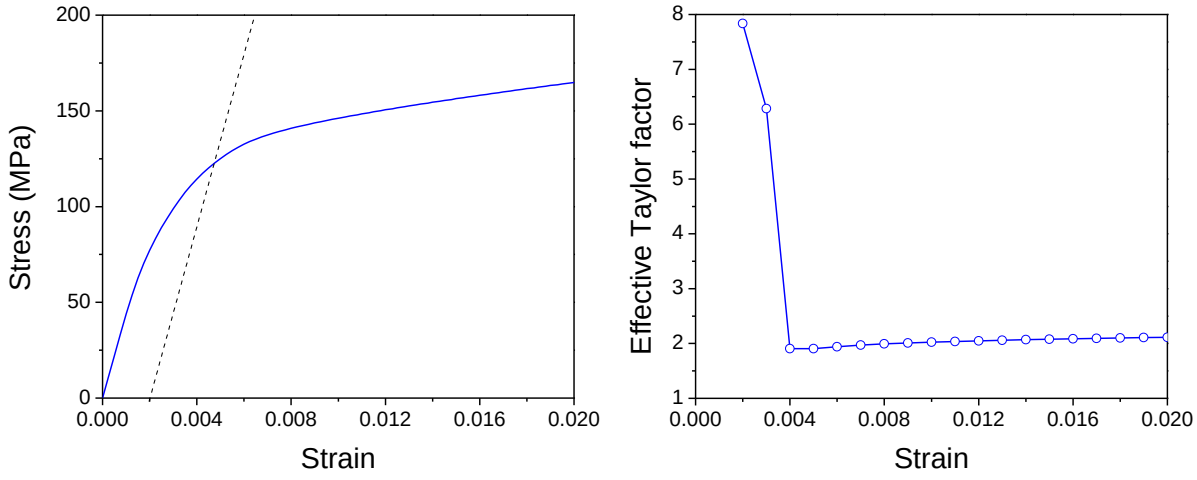

Figure 17. Representative EVPSC simulations of monotonic tensile deformation of a rolled Mg alloy sheet, highlighting the elastoplastic transition during which plastic strain accommodation shifts from being initially dominated by basal slip to a condition of polyslip involving basal and prismatic slip and even twinning.

Figure 18 shows the results of simulated strain rate jump tests with up-jumps and down-jumps between the rates 0.01, 0.001, and 0.0001 s^{-1}, with an initial strain rate of 0.001 s^{-1}. Figure 18(a) presents the stress-strain curve and Figure 18(b) shows the corresponding relative activity of the slip and twin modes.

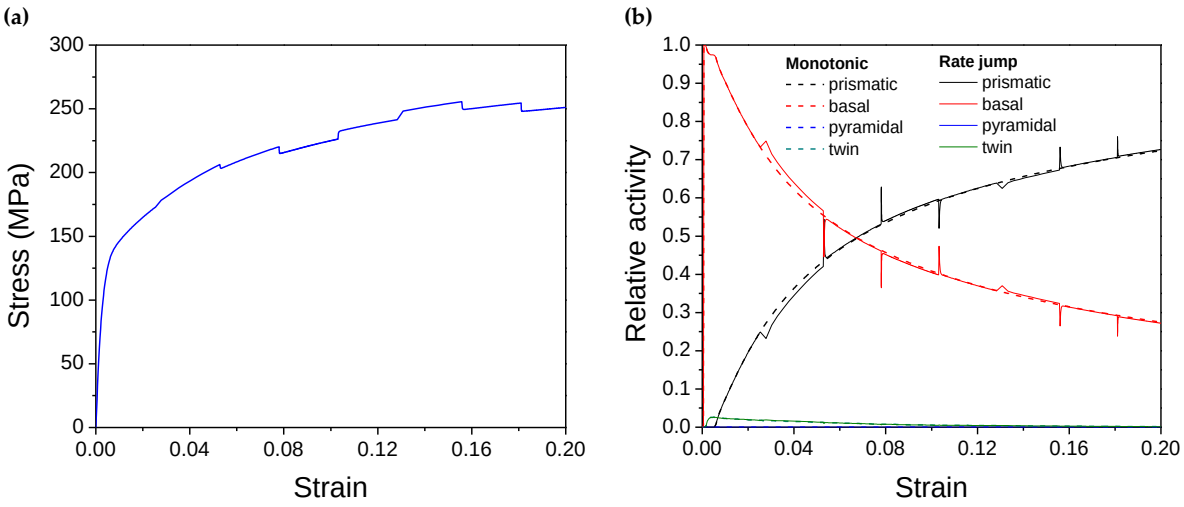

Figure 18. Representative elasto-viscoplastic crystal plasticity simulation results showing (a) the stress-strain curve and (b) slip and twin mode activities as a function of applied strain during strain rate up-jump and down-jump tests between the rates 0.01, 0.001, and 0.0001 s-1.

Figure 19 presents the results of a simulated repeated stress relaxation test. Figure 19(a) shows the stress as a function of time for this type of test, and Figure 19(b) shows the corresponding relative activities.

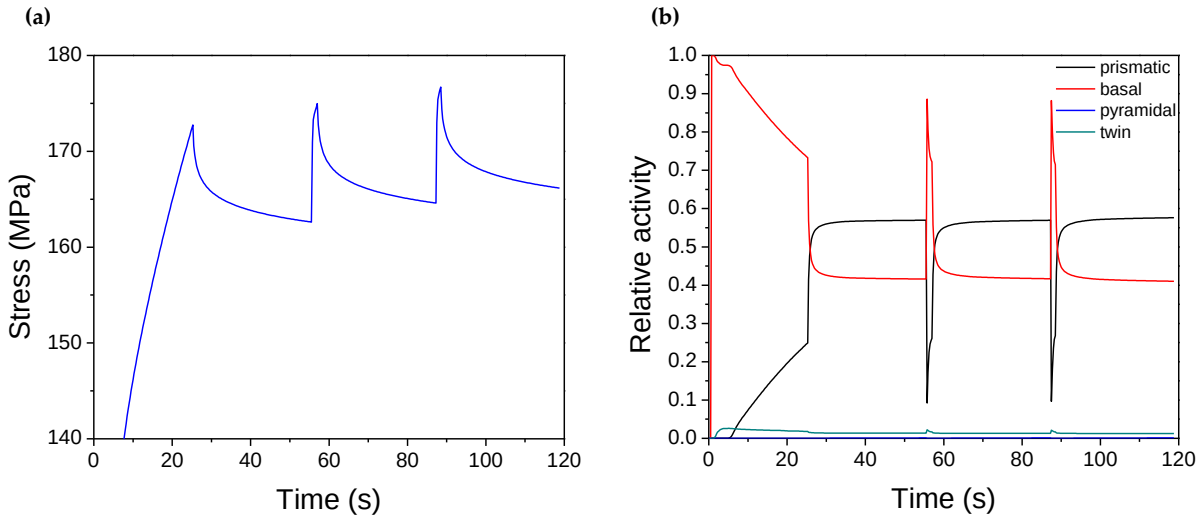

Figure 19. Representative elasto-viscoplastic crystal plasticity simulation results showing (a) stress relaxation and (b) slip and twin mode activities as a function of time during repeated stress relaxation tests.

3.3.3 Haasen Plot of polycrystalline binary Mg alloys

Tensile strain rate jump test data are used to compute the apparent polycrystalline activation volumes in the normal way. The inverse of these activation volumes is plotted against the flow stress due to strain hardening ($\sigma - \sigma_0$), where σ_0 is the tensile yield strength determined at 0.2% offset from the tensile tests data (i.e., the Haasen plot shown in Figure 20 for the different Y and Sc solute concentrations in Mg at 78 K). Only the cryogenic (78 K) data are presented here since the ambient temperature (298 K) showed evidence of DSA. The dependence of the inverse of activation volumes at yield (i.e., Haasen plot intercepts) and the SRS (the slope of the Haasen

plot multiplied with Mk_BT) on solute concentration was quantitatively determined using the data represented in Figure 20, and the results are shown in Figure 21.

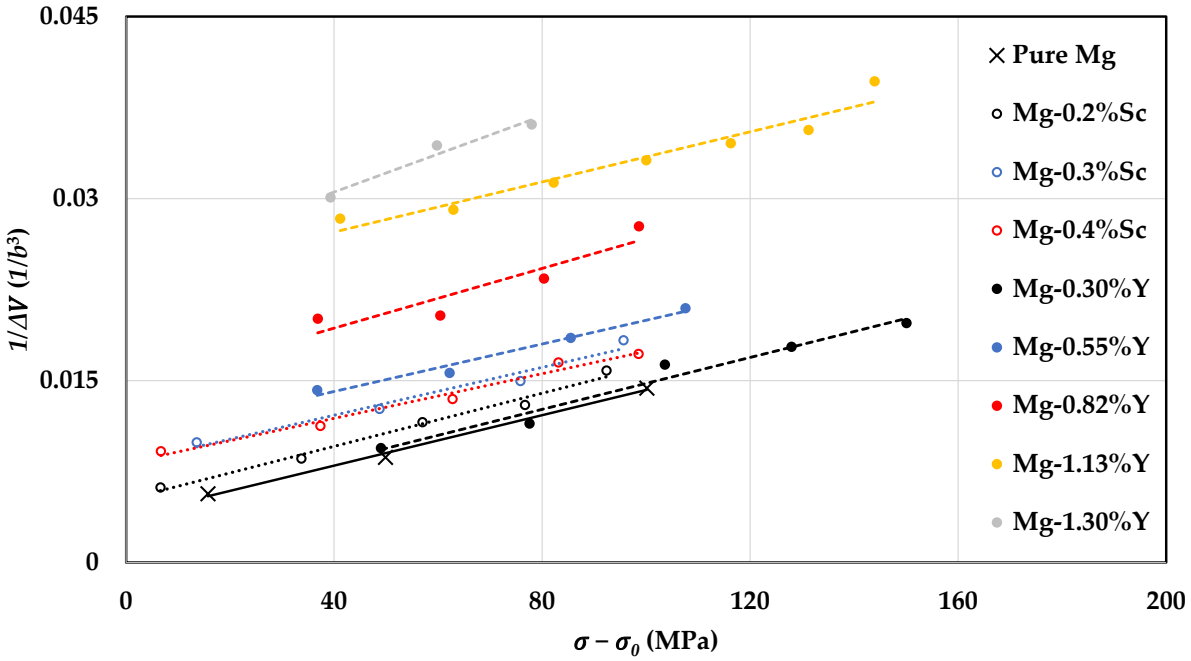

Figure 20. Combined Haasen plots for different Sc and Y solute concentrations in Mg, obtained from extracted data of tensile strain rate up-jump tests at 78 K [76-79].

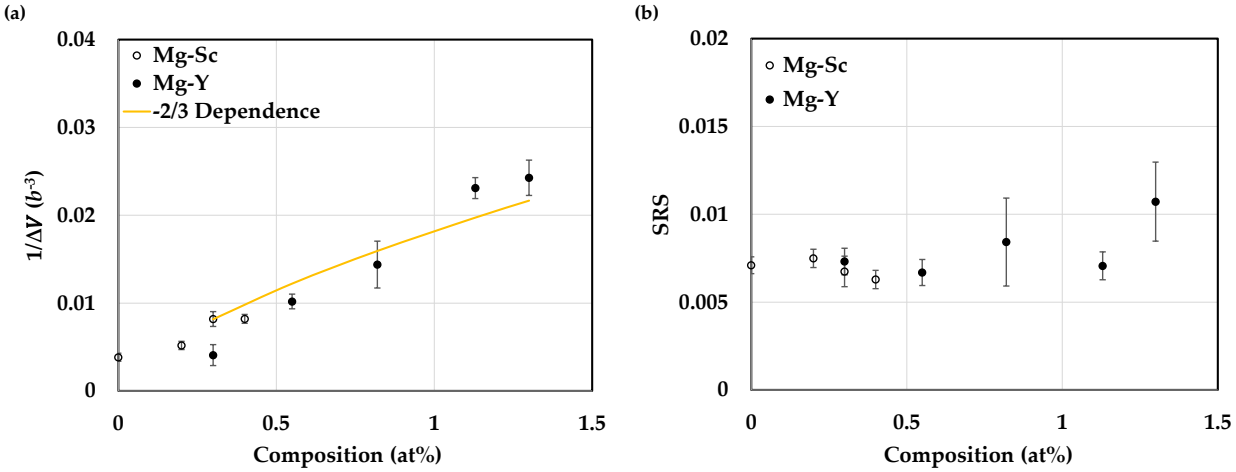

Figure 21. Haasen plot (a) intercepts and (b) slopes (SRS) for Mg-Sc and Mg-Y at 78 K.

3.4 Discussion

3.4.1 Polycrystal Plasticity Modelling

The results of the EVPSC simulations of monotonic tensile tests show that the effective Taylor factor evolves rapidly during the elastoplastic transition (yielding), beginning first at a high value because all of the plastic deformation is sustained by basal slip within crystals that are relatively poorly oriented to accommodate such deformation (due to the basal texture of the rolled sheets). This helps explain why some researchers have historically used high values of M in their considerations of Mg and its alloys [95,96,97,98]. However, by the time the material yields macroscopically, the *effective* Taylor factor has decreased to a level of $M \sim 2.1$, because a significant portion of the strain is being accommodated by twinning and prismatic slip of dislocations with the same <a> Burgers vector as those that glide on the basal planes. The value increases slightly with tensile deformation due to a modest texture evolution which renders the grains less favorably oriented for prismatic slip. Nevertheless, the value of $M \sim 2.1$ is deemed appropriate for analyzing all of the activation data of the present study. In particular, this value is not strongly sensitive to the relative strengths of the slip modes (which may vary slightly from one alloy to the next) or crystallographic texture (which may also vary slightly from one sample to the next).

The results of the strain rate jump test EVPSC simulations emphasize that the basal mode is dominant at low strain levels (<7% strain) after which prismatic slip becomes the primary strain carrier. In fact, a significant amount of the plastic strain is accommodated by basal slip during microyielding, as discussed in a previous study [99]. It is also evident that when there is a decrease in the strain-rate (during a down jump for example) the relative activity of prismatic slip increases.

On the other hand, the basal slip activity increases when the strain-rate increases as in the case of an up rate-jump. However, the relative activities of these two modes only momentarily change during the rate jumps, and immediately return to values very similar to those prior to the jump. Using the aforementioned analysis methods of Basinski [80] and Wagoner [81], these transient excursions in relative activity are not expected to influence the results of the experimental assessments of thermally activated plasticity.

As for the stress relaxation test EVPSC simulations, the results also reveal that the basal mode is dominant near yielding, however, the relative activity profile during stress relaxation significantly differs from that of the rate jump test. At the onset of relaxation, the prismatic activity sharply increases along with a corresponding decrease in the basal activity. Throughout the relaxation, the prismatic slip remains the major strain carrier. This is a direct consequence of the higher strength of the prismatic slip as compared to basal and is evident from the viscoplastic flow rule mentioned in Section 2.6, even if one assumes that both the modes have the same stress exponent. These results suggest researchers should exercise caution when employing stress relaxation tests to infer mechanistic insight in materials known to deform simultaneously by multiple mechanisms.

Finally, as mentioned in Section 2.6, the simulations were carried out to examine the behavior of these alloys collectively. The response of each alloy was not fitted individually. The initial texture employed in the simulations is representative of many textured Mg alloys. The strength and hardening parameters employed here are also typical of Mg alloys. The conclusions drawn from the simulations do not depend on the exact magnitude of the CRSS, as long as the rank order: $\tau_{basal} < \tau_{twin} < \tau_{prismatic} < \tau_{<c+a>}$ is maintained, and this is quite well-established in the literature

[84,100]. Thus, the conclusions drawn from the simulations are expected to be valid for a broad range of Mg alloys.

3.4.2 Composition dependence of thermal activation parameters

From Figure 20, the increase of the inverse activation volumes with rising flow stress during strain hardening is observed. In addition, the slope (which is proportional to the SRS) remains unchanged with straining. Such a response is adherence to a generalization of the Cottrell-Stokes (CS) law, mentioned in Section 2.3. Figure 21(a) reveals a similar trend of the intercept ($1/\Delta V$) with solute content for both Y and Sc. In agreement with the Labusch solute strengthening model, a $c^{2/3}$ dependency satisfactorily describes the Y data, though the best-fit relationship is admittedly closer to linear. It is not possible to assess the composition dependence for Sc because of the very low solubility of Sc in Mg [101]. In Figure 20, it is vivid that the slopes remain essentially constant across different Y or Sc solute concentrations. Figure 21(b) shows that the corresponding SRS is insensitive to the level of alloy content for both Y and Sc (it lies between ~ 0.006 and 0.008 over the entire range of compositions explored). This observation provides further support for the generalized CS law and suggests a simple linear superposition rule [102]:

$$\frac{1}{\Delta V} = \frac{1}{\Delta V_{solute}} + \frac{1}{\Delta V_{dislocation}} \qquad \text{Eq. 17}$$

The slight deviation for 1.30 at% Y may be attributed to statistical uncertainty and insufficient measurements for this solute concentration.

3.4.3 Stress Equivalence

As a first look into the principle of stress equivalency, the data recently reported by Miura et al. [42] for the single crystal Mg-Zn, Mg-Y, and Mg-Dy alloys and the current experimental data for polycrystalline Mg-Sc [76,77] and Mg-Y [78,79] were added to Basinski's original plot of stress equivalency of Mg alloys oriented for basal slip. Like previous studies, Miura et al. [42] had collected flow curves at 78 and 200 K from single crystals oriented for basal slip, so it was straightforward to demonstrate that their data followed the same curve as the data collected by Basinski et al. [30]. On the other hand, the polycrystal flow stresses had to be resolved onto the individual slip systems using the aforementioned Taylor factor and the contribution of grain boundary strengthening to the strength at 78 K had to be taken into account. Additionally, the present data from polycrystalline Mg-Y and Mg-Sc were obtained at 78 K and 298 K, rather than 78 K and 200 K. Nevertheless, the fact that all of the polycrystalline data were observed to lie on a *similar* curve (not shown as the 298 K data are not in the scope of this current work) to that originally proposed by Basinski et al. motivated further investigation. This further investigation relies upon two aspects: (i) in addition to the flow stresses, the activation volumes of the polycrystalline alloys at 78 K are known and (ii) models exist which enable prediction of the flow stress at any temperature or strain rate within a specified regime (e.g., Eq. 9 & Eq. 10).

The approach, based upon the Leyson and Curtin [35,36] model, was first tested using the single crystal Mg-Zn data at 78 K of Akhtar and Teghtsoonian [16], who had reported both the flow stresses and activation volumes at 78 K and 200 K, whereas Basinski et al. employed only the difference in the flow stresses in their original comparison. Here, we show that this difference may be predicted using knowledge of the activation volumes and a reliable model. First, it is noted

that the activation volumes reported by Akhtar and Teghtsoonian [16] assumed an "athermal stress" component (τ^G), because researchers had noted an "athermal plateau" in flow stresses above a certain temperature, beyond which the change in flow stress is attributed to the reduction in the relevant shear modulus of the material with rising temperatures. As such, they typically reported activation volumes as a function of the thermal stress, τ^*, obtained with a variety of methods [103,104] designed to remove the athermal portion τ^G from the applied stress $\tau^* = \tau - \tau^G$. In 2012, Leyson et al. [38] proposed that such a stress is not truly "athermal" and that Mg alloys, in particular, are subject to distinct energy barriers, which result from basal dislocation core spreading. In the high temperature-low stress regime, the higher energy barrier dominates, and thus leads to a weak dependence of the stress on temperature. Per this assertion of Leyson et al., the activation volumes of the Mg-Zn single crystal alloys oriented for basal slip [16] have been recalculated without the assumption of an "athermal" stress (see Table 2). With these data, one can combine Eq. 9 and Eq. 10 to determine the mechanical threshold stress τ_{y0} for a given alloy using all the known parameters at a temperature T_1. This is demonstrated for the case of the intermediate stress regime $\left(0.2 < \frac{\tau_y(T)}{\tau_{y0}} < 0.5\right)$ as follows:

$$\tau_{y0} = \tau_{y,T_1} \exp\left(\frac{k_B T_1}{\Delta V_{T_1} \tau_{y,T_1}} \ln\left(\frac{\dot{\varepsilon}_0}{\dot{\varepsilon}}\right)\right) \qquad \text{Eq. 18}$$

If one substitutes this value back into Eq. 9, the value of τ_y can be predicted at any temperature T_2 within the corresponding regime using the data obtained at T_1:

$$\tau_{y,T_2} = \tau_{y,T_1} \exp\left(\frac{k_B(T_1 - T_2)}{\Delta V_{T_1} \tau_{y,T_1}} \ln\left(\frac{\dot{\varepsilon}_0}{\dot{\varepsilon}}\right)\right) \quad \text{Eq. 19}$$

The same sort of analysis can be performed for the other strength regimes. In each case, the resulting flow stresses are compared against the implied mechanical threshold stress to confirm the appropriate regime is employed. However, the low stress regime is not of particular interest in the present study of polycrystalline Mg-rare earth element alloys and the flow stresses predicted by the intermediate and high stress models are similar.

Figure 22 shows all of the data originally reported by Basinski et al. [30] in grey, along with values for single crystal Mg-Zn, Mg-Y and Dy reported by Miura et al. [42], the results of our reanalysis of the single crystal Mg-Zn alloys of Akhtar and Teghtsoonian [16], along with our analysis of polycrystalline Mg-Y and Mg-Sc, which is described below. Notice that the Mg-Zn data reanalyzed using the model for the intermediate stress regime (blue circles) essentially overlaps with the data provided on the original Basinski plot (blue-grey circles), except at the lowest stresses. The difference $(\tau_y(78\,K) - \tau_y(200\,K))$ is overpredicted for the lowest stress cases because it falls outside the applicable intermediate strength regime in those cases. Since the low stress regime is outside the present interest, no further analysis was performed on these data. In principle, one could employ the full Leyson-Curtin model [35] to interpret such cases.

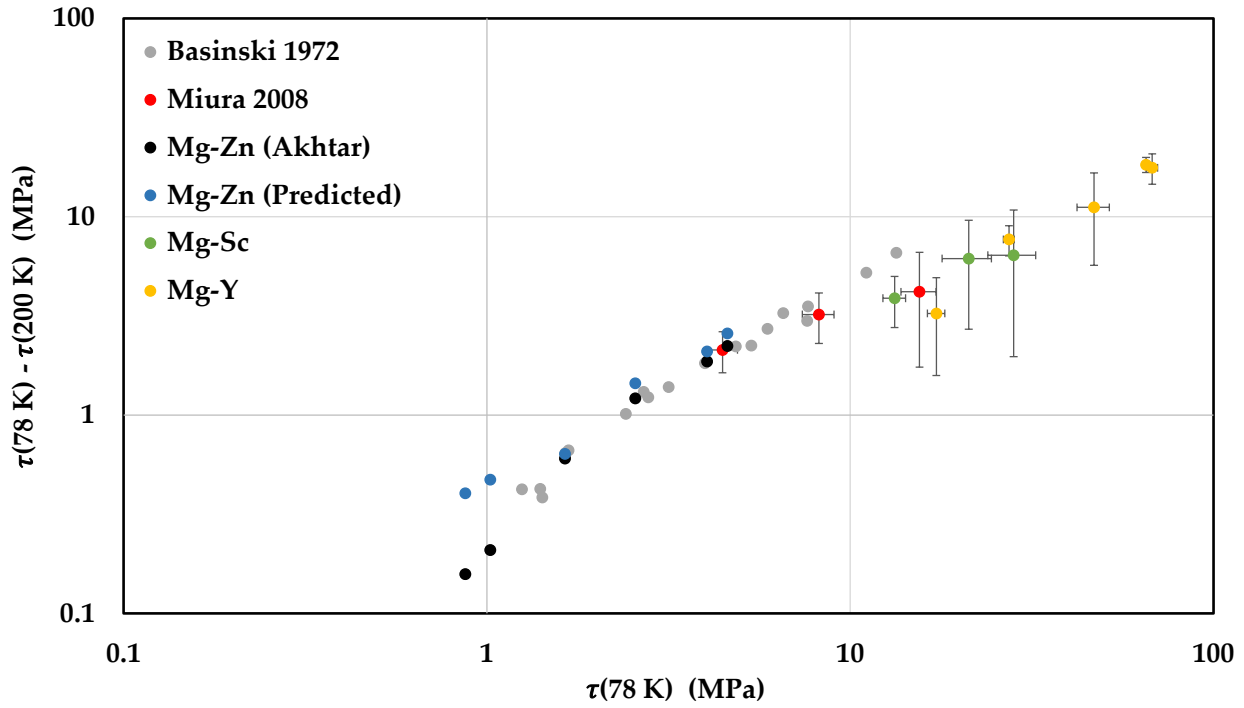

Figure 22. "Basinski plot" with reanalyzed data from single crystal Mg-Zn (blue circles), along with new data from single crystals (Miura et al. 2008) and polycrystalline Mg-Y and Mg-Sc.

Incorporation of the modern data from Miura et al. [42] suggests the possibility that the curve describing stress equivalence plot may have a lower slope than original suggested, at the highest stress levels. Note that the two highest strength alloys examined by Basinski et al. [30] were Mg-Li alloys with much higher solute concentrations (11.8 and 15 at.%, respectively) as compared to all of the other alloys in the plot. Even the original authors, Urakami, Meshii and Fine [105,106], suggested the possibility of solute clustering in these alloys, which may explain why their behavior might be somewhat exceptional, relative to other alloys in which the probability of solute clustering is lower.

Table 2. Reported values of τ_y at 78, 200 K for Mg-Sc, Mg-Y, and Mg-Zn alloys with the corresponding ΔV (b = Burgers vector for basal slip). Values obtained from the Miura et al. [42] are also provided for different solute species. *Note: Entries with (*) sign represent predicted values at the mentioned temperature.*

Solute		**Composition (at.%)**	ΔV **(b^3)**	$\tau_y(78\ K)$ **(MPa)**	$\tau_y(200\ K)$ **(MPa)**	$\tau_y(78\ K) - \tau_y(200\ K)$ **(MPa)**
Zn		0.006	1685.0	0.9	0.7 (0.5 *)	0.2 (0.4 *)
		0.019	1438.2	1.0	0.8 (0.5 *)	0.2 (0.5 *)
		0.054	1130.5	1.6	1.0 (1.0 *)	0.6 (0.6 *)
		0.15	427.2	2.6	1.3 (1.1 *)	1.2 (1.4 *)
		0.258	308.6	4.0	2.2 (1.9 *)	1.9 (2.1 *)
		0.45	240.5	4.6	2.4 (2.0 *)	2.2 (2.6 *)
Sc		0.2	197.3	13.3	9.4 *	3.9 *
		0.3	115.0	28.2	21.8 *	6.4 *
		0.4	119.0	21.2	15.0 *	6.2 *
Y		0.3	213.0	17.3	14.0 *	3.3 *
		0.55	98.5	27.4	19.7 *	7.7 *
		0.82	66.3	46.9	35.8 *	11.1 *
		1.13	46.6	67.9	50.2 *	17.7 *
		1.3	42.0	65.2	46.9 *	18.3 *
Miura	Zn	0.5	—	4.4	2.3	2.1
	Dy	0.5	—	8.2	5.0	3.2
	Y	1	—	15.5	11.3	4.2

In order to determine if polycrystals also adhere to the principle of "stress equivalence," it is necessary to resolve the stress onto the slip planes using the aforementioned Taylor factor $\tau_{rss} = \sigma_0/M$ and then remove the (Hall-Petch) grain size strengthening (τ_{gs}) contribution from the overall CRSS, leaving only the effects of lattice resistance and solute strengthening:

$$\tau_y = \left(\sigma_0 - k/\sqrt{d_g}\right)/M \qquad \text{Eq. 20}$$

Ono et al. [107] provide information regarding the temperature dependence of the Hall-Petch parameter k in pure polycrystalline magnesium, revealing k = 12.47 MPa$\sqrt{mm}$ at 78 K. Some researchers have suggested that the grain size (d_g) effect may be dependent upon solute concentration as well [108]. However, these effects have an insignificant impact at small solute concentrations currently of interest, and it is therefore preferable to associate all the solute interactions with dislocation mobility instead. The results of this analysis are reported in Table 3.

Table 3. Reported values of CRSS, τ_{gs} (resolved grain size strengthening), and τ_y at 78 K for polycrystal Mg-Sc and Mg-Y alloys.

Solute	**Composition (at.%)**	**Grain Size (mm)**	$\boldsymbol{CRSS\ (78\ K)}$ **(MPa)**	$\boldsymbol{\tau_{gs}(78\ \mathrm{K})}$ **(MPa)**	$\boldsymbol{\tau_y(78\ K)}$ **(MPa)**
Sc	0.2	0.052	39.3	26.0	13.3
	0.3	0.059	52.6	24.4	28.2
	0.4	0.061	45.2	24.0	21.2
Y	0.3	0.170	31.7	14.4	17.3
	0.55	0.170	41.8	14.4	27.4
	0.82	0.124	63.8	16.9	46.9
	1.13	0.132	84.2	16.3	67.9
	1.3	0.075	86.9	21.7	65.2

It is noted that Basinski et al. did not seek to parse the contributions of lattice resistance and solute strengthening in their analysis of the thermally activated behavior of FCC and HCP alloys. This may have been motivated by their knowledge of the fact that octahedral slip within pure FCC metals and basal slip within pure HCP metals, is small and rather rate insensitive. In the present polycrystalline HCP metal context, where some non-basal slip is inevitable, this choice raises important questions about how the intrinsic rate sensitivities of distinct deformation modes superpose, in addition to the previously explored question of how the rate sensitivities of distinct obstacles to a single deformation mode superpose [109,110].

With these values of $\tau_y(78\ K)$ and the activation volumes at yield (Figure 21(a)), the stress differences $\tau_y(78\ K) - \tau_y(200\ K)$ required to construct the "Basinski plot" from polycrystalline data can be computed in the same way as was demonstrated above for single crystal Mg-Zn (see Table 2). The final results are presented in Table 2 and Figure 22, complete with error bars corresponding to propagation of experimental uncertainties, showing that even data obtained from textured polycrystalline Mg alloy samples conform to the principle of stress equivalence, which was originally demonstrated using data from Mg single crystals oriented for basal slip. As suggested earlier, it mattered little whether the model of the high or intermediate stress regimes were employed to predict the flow stress at $\tau_y(200\ K)$ since even the highest $\tau_y(78\ K)$ stress levels are in the range $\left(0.4 < \tau_y(T)/\tau_{y0} < 0.6\right)$ where the two models closely overlap [35]. It is noted that one of the coauthors used a somewhat different value of M = 2.88 for the effective Taylor factor in previous studies [76,78]. Indeed, there is much controversy in the literature regarding the most suitable Taylor factor for hcp materials. Interestingly, however, variation in the effective Taylor factor simply shifts the data along a straight line (i.e., the slope does not change). Because the slope is close to unity over the entire range of interest, adherence to the principle of stress equivalence is revealed insensitive to the choice of Taylor factor for in plane tensile deformation of basal-textured Mg alloys.

One aspect to note is the difference between the single crystal Mg-1%Y data point and the data obtained from polycrystals of similar composition, e.g., Mg-0.82%Y and Mg-1.13%Y. The discrepancy between the two is hypothesized as being due to the activity of non-basal slip modes discussed earlier in this section, especially since there is no reasonable value of Taylor factor which can be used to reconcile the two datasets. In this study, the 0.2% offset yield strength was employed and it was shown that the effective Taylor factor reaches a stable value at this strain level (Figure

17). On the other hand, one could employ a much smaller offset, closer to the proportional limit, where only basal slip is activated (Figure 18 and Figure 19). In such cases, one would have to account for the fact that the Taylor factor is rapidly evolving.

Finally, when Basinski et al. [30] originally reported the principle of stress equivalence, they did not have activation volume data for many Mg alloys. Hence, they used the CRSS differences $\tau_y(78\,K) - \tau_y(200\,K)$ which were available in the literature for their initial assessment. It is now possible to plot the corresponding activation volumes at yield for Mg-Zn (single crystal), Mg-Y and Mg-Sc against $\tau_y(78\,K)$, as shown in Figure 23. These data suggest a rather simple relationship between ΔV and τ_y, regardless of solute type or concentration. As mentioned previously by Leyson and Curtin, [35] it is more straightforward to predict the flow stresses than the activation volumes which represent the slope of the activation free energy vs. flow stress. Among other aspects, they highlight the fact that slight differences in the assumed dislocation line tension can have a significant effect upon the predicted activation volume. Thus, although the values of ΔV predicted via atomistic simulation do not agree precisely with experimental observations, the slope (power law exponent) is essentially identical to it, implying that the stress dependence of this parameter is accurately predicted. We find it interesting that this is true even for the lowest stress cases of dilute Mg-Zn.

Here, "stress equivalence" means that a single measurement of the flow stress at 78K can be used to infer the activation volume. Using this information together with the comprehensive model of solute strengthening (Eq. 9 & Eq. 10), one can predict the flow stress over a wide range of strain rate and temperature. The fact that the single crystal and polycrystal results lie on a single curve (in both Figure 22 and Figure 23) suggests that the thermally activated mechanisms which

control basal slip in oriented single crystal alloys are the same ones which control yield in polycrystals. This is consistent with the polycrystal simulations discussed earlier, which showed that basal slip is the dominant strain carrier during the initial stages of yielding. That said, it is emphasized that polycrystals invariably have some deformation on other slip systems. Again, the resulting "forest dislocation" interactions could explain why the present flow stress values are high, even though the effects of grain strengthening have been removed. The effect of these forest dislocation interactions appears to contribute to the overall thermally activated response rather simply (Eq. 17), leading to the interesting observation that the strain rate sensitivity is constant with straining, regardless of whether basal or prismatic slip is dominant.

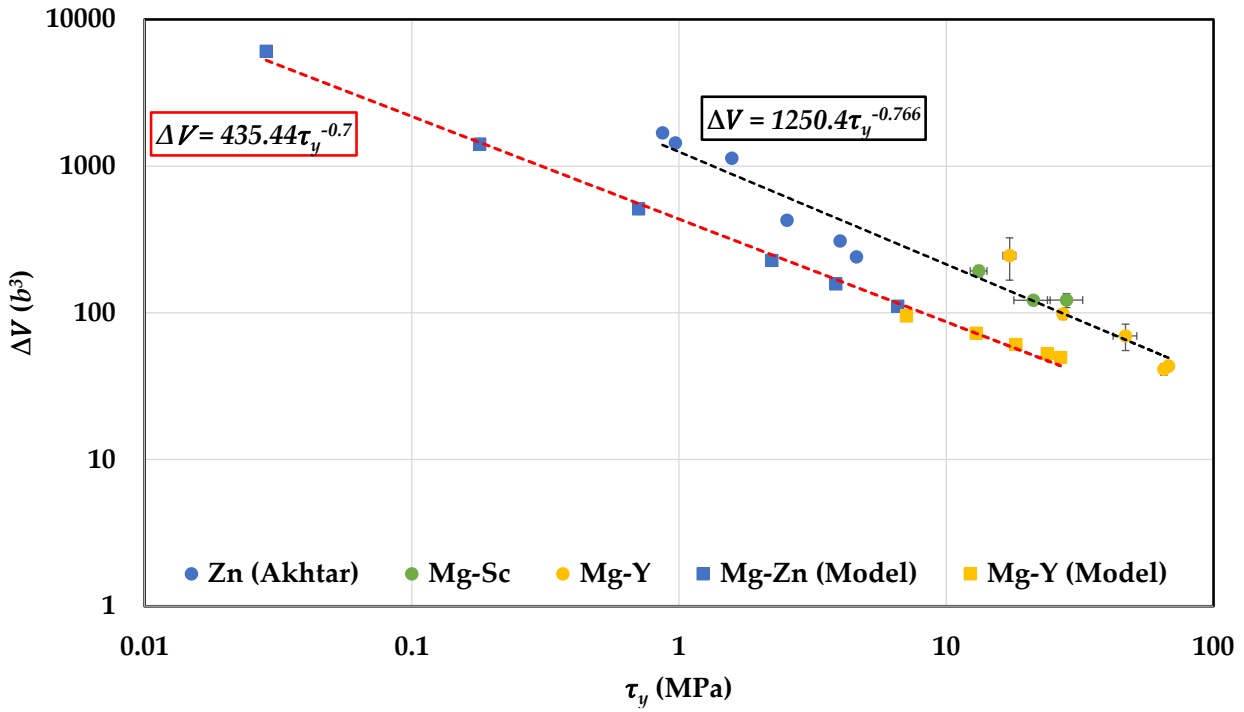

Figure 23. An alternative presentation of stress equivalence, presented as a log-log plot of the ΔV values against the corresponding $\tau_y(78\ K)$. The upper curve corresponds to the experimental data of this study, whereas the lower curve are predictions of the Leyson-Curtin model.

3.5 Conclusions

1. EVPSC (elasto-viscoplastic self-consistent) polycrystal plasticity simulations indicate that the dominant slip mode during tensile microyielding of these textured polycrystalline Mg alloys is basal slip. However, non-basal mechanisms (especially prismatic slip) are activated during macroyielding. Correspondingly, the *effective* Taylor factor very quickly approaches a value which remains rather constant throughout the tensile test.

2. The EVPSC results also indicate that the steady-state change in relative slip activity during strain rate jump tests is small for the rate jump magnitudes typically enforced experimentally. That is, the relative slip activities quickly return to values close to the original magnitude after a transient response associated with the strain rate change.

3. EVPSC polycrystal plasticity simulations for repeated stress relaxation tests indicate that the change in relative slip activity is significant and does not return to the original magnitude. Thus, caution should be exercised when interpreting the results of stress relaxation tests performed on materials that deform by multiple mechanisms at once.

4. The experimental results show that the generalized Cottrell-Stokes law (the strain rate sensitivity is insensitive to strain hardening) holds for textured, polycrystalline, binary Mg alloys deformed in tension. It is hypothesized that the rate controlling mechanism is related to basal-prismatic forest dislocation interactions, regardless of which mode dominates strain accommodation.

5. The principle of “stress equivalency” originally introduced in the context of oriented single crystals is shown to also hold for tensile deformation of basal textured polycrystalline Mg alloys. Notably, this conclusion is insensitive to the choice of Taylor factor because the slope of the Basinski plot is close to unity over the range of interest. This means that changing the Taylor factor would only result in shifting the data points together along the same straight line; meaning that the stress equivalence principle still holds for different Taylor factors.

6. This means that once the yield strength of an alloy at a low temperature is known, the activation volume at yield can be directly predicted. With this activation volume, the flow stress can be predicted at any other temperature or strain rate, provided one employs the appropriate model for the rate and temperature regime of interest.

Chapter 4: Transitioning from Static to Dynamic Solute Effects

This chapter represents a transition from the focus on static solute effects to discussion of dynamic solute effects. In Chapter 3, the investigation revolves around thermal activation of dislocations in under static solute conditions. This means that the mobility of the solutes may be ignored relative to the motion of the solute. For the different polycrystalline Mg-Sc and Mg-Y alloys investigated, it was shown that these conditions only prevail at cryogenic temperatures. As demonstrated in that chapter, the stress equivalence principle was shown to apply to textured, polycrystalline, binary Mg alloy sheets deformed in tension along the sheet rolling direction. These alloys also abide by the generalized Cottrell-Stokes (CS) law and have a positive strain rate sensitivity (SRS). As discussed in Section 2.3, the generalized CS law states that — for two different strain rates at a specified temperature — a difference between flow stresses does not depend on strain hardening. However, the data reported [77,79] for polycrystalline Mg-Sc and Mg-Y do not follow the generalized CS law and deviate from the positive SRS reaching negative values (i.e., indicating the presence of DSA) when deformed in tension at ambient temperature. In other words, the SRS decreases with straining at room temperature, as shown in Figure 24. This phenomenon introduces additional complexities which influence the activation volumes and their overall deformation behavior. The simple linear superposition rule (Eq. 17) is not expected to apply in such cases.

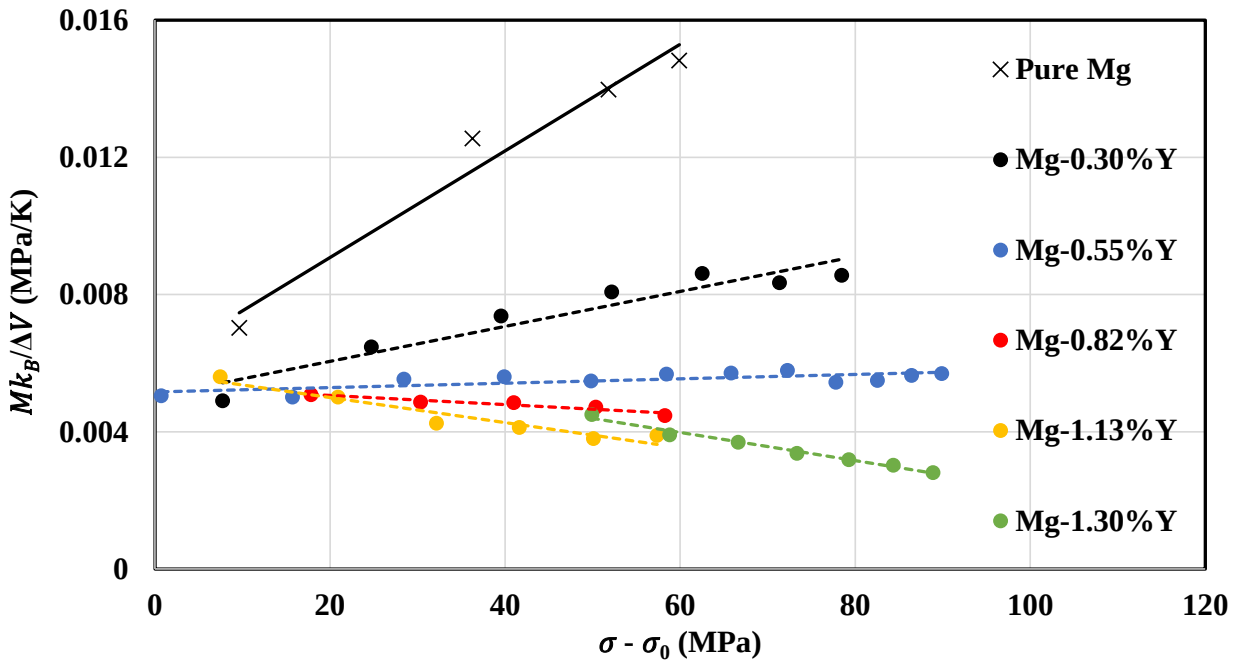

Figure 24. Haasen plot for different Y solute concentrations in Mg, obtained from extracted data of tensile strain rate up-jump tests at 298 K [79].

In short, these observations highlight the fact that the principle of stress equivalence does not hold in the presence of DSA. As discussed in Section 2.5, the modelling of the shear yield strength and the flow stress stands within the framework of static solute effects. Therefore, the analysis approach performed in Chapter 3 cannot be simply applied on the polycrystalline Mg-Sc and Mg-Y data deformed in tension at room temperature. Rather, it is important to first have a better understanding of the contributions of solute and forest dislocations to DSA, which is the topic that is discussed in Chapter 5.

Chapter 5: Part II – Effects of Dynamic Solute on Dislocation Motion – Focusing on Junction Formation

Previous studies have attempted to explain the dislocation-dislocation interaction contribution to DSA — in FCC materials — in terms of formed Lomer-Cottrell locks. In one of those studies [111], Picu used the energy minimization approach of the anisotropic dislocation line tension model to determine the dependency of the sessile junction formation on the amount of solute cluster pinning the forest dislocation. Other studies [60,62] that preceded Picu's reported yield surfaces for the case of Lomer-Cottrell locks and showed dependency on the initial configuration of the interacting dislocations. These yield surfaces represent the breakaway stress from formed junctions (i.e., the strength of junctions). Picu took this approach further by determining the breakaway stress in the presence of solutes along the forest dislocation (analogous to a formed Cottrell atmosphere). The power of this simple anisotropic dislocation line tension model stood out when it was confirmed that similar results to Picu's approach could be achieved using more sophisticated models such as discrete dislocation dynamics (DDD) [112]. Therefore, it is reasonable to use this model to explore the nature of DSA.

5.1 Line Tension Modelling

As discussed in Section 2.9, Eq. 13-Eq. 16 are the base equations for this model. The application of these formulations can be extended from a dislocation line pinned at two fixed ends to a system of interacting dislocations. Figure 25 is a schematic representation of the problem under current study in which these equations are used to determine the junction formation length as well as the breakaway stress. Figure 25(a) shows two initial straight dislocations — one mobile (denoted by m) and one forest (denoted by f) — in a crossed state in an FCC crystal structure, where the initial length of both dislocations is $2L$.The mobile dislocation has a Burgers vector $\vec{b}_m$ of $\frac{1}{2}[\bar{1}10]$ and lies in the (111) plane while the forest dislocation has a Burgers vector $\vec{b}_f$ of $\frac{1}{2}[101]$ and lies in the $(\bar{1}11)$ plane. The junction direction is simply the cross product the two slip planes — $[0\bar{1}1]$, and its Burgers vector $\vec{b}_j$ is the summation of $\vec{b}_m$ and $\vec{b}_f$. The character angle of each dislocation is denoted by α_m and α_f for the mobile and forest dislocations, respectively. The initial configuration of a dislocation is defined as the angle between the initial dislocation line and the junction direction. For the mobile dislocation, it is denoted by ϕ_m while it is ϕ_f for the forest dislocation. The mobile dislocation is pinned at points A and B while the forest dislocation is pinned at points C and D.

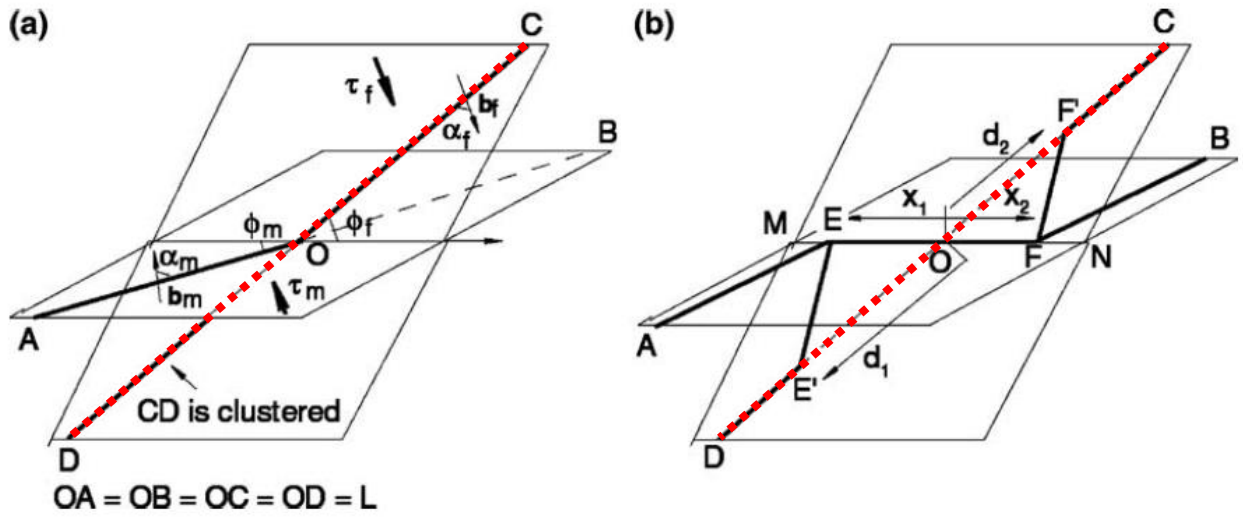

Figure 25. A schematic representation [111] of the Lomer-Cottrell lock problem. The red dashed line represents the forest dislocation being pinned by solute in (a) the initial configuration of the dislocations and (b) the final equilibrium configuration.

As mentioned earlier, the energy approach to represent the amount of solute the pinning the forest dislocation is denoted by a variable Q as the binding energy per unit length of the forest dislocation to its cluster. Varying Q will influence the final equilibrium shape of the system of dislocations. Due to the symmetry of the initial configuration, it is possible to divide the setup into two geometric portions. The equilibrium shape is then defined by the variables x_1, x_2, d_1, and d_2, where x represents the length along the junction that has formed and d represents the length along the initial forest dislocation that has escaped from its solute cluster. From the schematic in Figure 25(b), these variables are defined geometrically as

- $x_1 \rightarrow$ OE,
- $x_2 \rightarrow$ OF,
- $d_1 \rightarrow$ OE',
- and $d_2 \rightarrow$ OF'.

5.1.1 Angle relationships

One of the essential components of this model that seems to be neglected for thorough discussion in the literature is the angle relationships. More precisely, the relationship between the angles α and ϕ. If this model were to be used without determining this important relationship, the results would not be reproduced as to what is reported in the literature. In this section, a thorough discussion regarding this matter is provided in an effort to fill in this gap.

In problems similar to the one under investigation, it is recommended that an accurate three-dimensional (3-D) schematic is drawn to have a better view and understanding of its geometry. This representation is shown in Figure 26. In this figure, $\vec{t}_m$ and $\vec{t}_f$ are the initial mobile and forest dislocation line directions, respectively. ζ_m and ζ_f are the angles between the junction direction ($\boldsymbol{x}$) and the Burgers vectors of the mobile and forest dislocations, respectively.

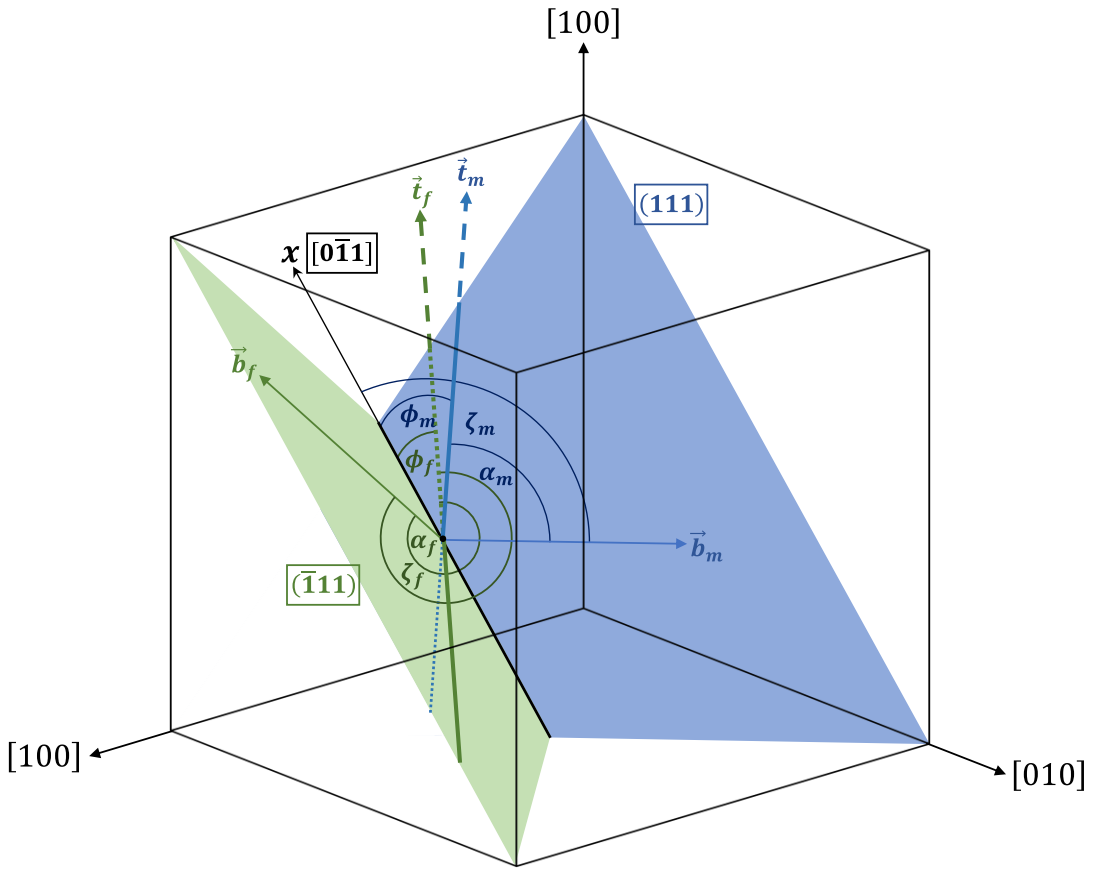

Figure 26. A 3-D schematic of the junction formation problem. The blue colors represent the mobile dislocation and its plane while the green colors represent the forest dislocation and its plane.

After the schematic drawn, it is important to check the relationships between the angles α, ϕ. Ultimately, the goal is to compute the angle ζ to determine α since ϕ is already an input parameter. First, it is possible to relate each dislocation's reference frame to the junction reference frame using the corresponding slip plane normal ($\hat{n}_m$ and $\hat{n}_f$). Using the right-hand-rule $\hat{n}_m$ and $\hat{n}_f$ are defined as

$$\hat{n}_m = \hat{x} \times \hat{y}_m = \hat{e}_m \times \hat{b}_m \qquad \text{Eq. 21}$$

$$\hat{n}_f = \hat{x} \times \hat{y}_f = \hat{e}_f \times \hat{b}_f \qquad \text{Eq. 22}$$

where $\hat{x}$ is the normalized junction direction — the one direction that is common between all three reference frames (of the mobile, forest, and junction dislocations). $\hat{y}_m$ and $\hat{y}_f$ are the directions orthogonal to both $\hat{x}$ and the corresponding slip plane normal, $\hat{b}_m$ and $\hat{b}_f$ are the unit Burger vectors of the mobile and forest dislocations, respectively, and $\hat{e}_m$ and $\hat{e}_f$ are the directions orthogonal to both corresponding plane normal directions and Burgers vector of the mobile and forest dislocations. Now that the vector relationships are defined, the schematics showing these vectors are shown for the mobile and forest dislocations in Figure 27. It can be seen from this figure that the angle relationships are

$$\alpha_m = \zeta_m - \phi_m \qquad \text{Eq. 23}$$

$$\alpha_f = \zeta_f - \phi_f \qquad \text{Eq. 24}$$

where ζ_m and ζ_f can be computed using the dot product between the junction direction and the mobile and forest dislocation line directions, respectively. In this case, $\zeta_m = 120°$ and $\zeta_f = 300°$. As for the character angle of the formed junction α_j, it can be computed using the dot product rule between the junction line direction and its Burgers vector. For Lomer-Cottrell locks, $\alpha_j = 90°$.

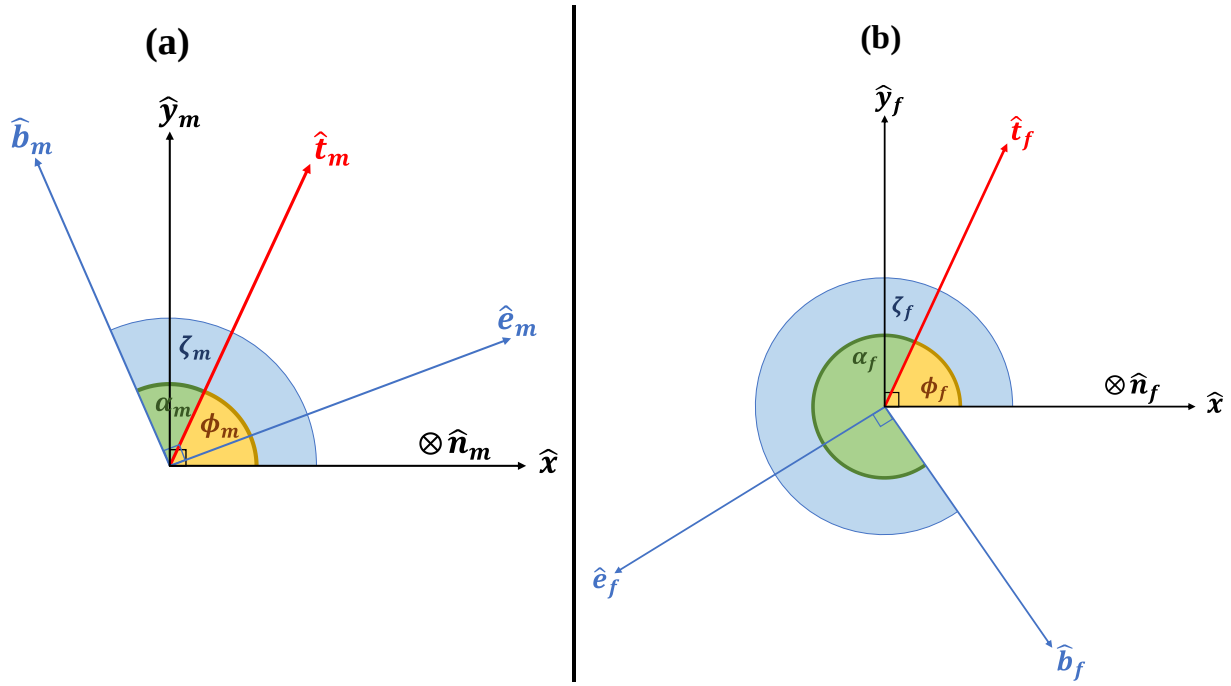

Figure 27. A detailed schematic showing the angle relationships for the (a) mobile and (b) forest dislocations.

5.1.2 Dislocation bow-out

Throughout the literature, the shape of a dislocation is usually taken as a near-elliptical arc bow out when subjected to some stress τ. The relationship between τ and the shape of the dislocation bow-out arc is

$$\tau = \frac{r\mu b}{4\pi a_1}\ln\left(\frac{R}{r_0}\right) \qquad \text{Eq. 25}$$

where r is the ratio between the major (a_1) and the minor (a_2) semiaxes of the ellipse (i.e., $r = a_1/a_2$). To integrate this shape into Eq. 13 and Eq. 15, a separate frame of reference must be used [113,114]. This reference frame takes the triple point (i.e., the endpoint connecting the junction

and the mobile and forest dislocation arms) as the origin while the other endpoint (i.e., pinning point) of the bowed-out dislocation arm as some point (X, Y). Using , the equation of the ellipse in this reference frame is

$$\frac{X^2}{a_1^2} + \frac{Y^2}{a_2^2} = 1 \qquad \text{Eq. 26}$$

The incremental self-energy of that dislocation arm is then defined as

$$dE(\alpha + \psi) = E(\alpha + \psi)\frac{\cos(\beta)}{\cos(\psi)}du \qquad \text{Eq. 27}$$

where ψ is the bow-out angle, β is the angle between the straight line connecting the endpoints of the bowed-out dislocation arm and the junction direction, and du is the incremental distance displaced by the triple point toward point O. These angles are required because they account for the change in the character angle of each dislocation segment as the dislocation arm bows out.

The same procedure applies to the dissipative work done by a dislocation as it sweeps an infinitesimal area in the slip plane. This area is then defined as

$$dS_A = X_h E(\sin(\beta) + \tan(\psi)\cos(\beta))du \qquad \text{Eq. 28}$$

where X_h is half the length of the straight line connecting the triple point to the pinning point of the bowed-out dislocation. Thus, Eq. 15 becomes

$$W = \int_{\Gamma} \tau b \, dS_A \qquad \text{Eq. 29}$$

According to Schoeck and Frydman [114], the angle ψ is defined mathematically as

$$\psi = \arctan\left(\left.\frac{dY}{dX}\right|_{X=X_h}\right) \qquad \text{Eq. 30}$$

Figure 28 is a simple geometrical representation of these angles for the mobile dislocation segment BF. Similarly, Eq. 30 can be applied to the forest dislocation segment FF' if there was some bowing out included (i.e., if there is an applied resolved shear stress τ_f in the plane of the forest dislocation).

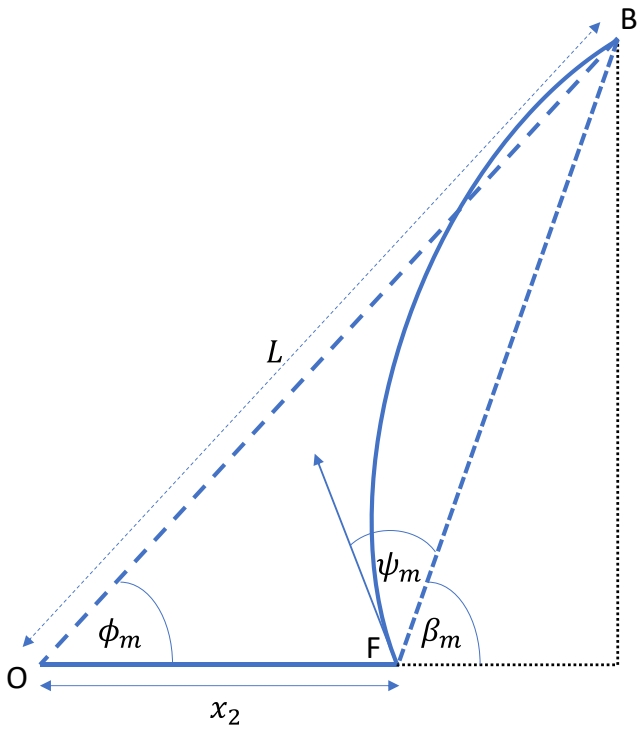

Figure 28. A geometrical schematic representing the angles used in Eq. 27 and Eq. 28 for the mobile dislocation segment BF.

The derivation of the angle β is a slightly different between the mobile and forest dislocation segments involved (BF and FF'). To illustrate this derivation, Figure 29(a) and Figure 29(b) show the geometrical relationships involving the variables x_2 and d_2 and the angle ϕ for both the mobile and forest dislocation portions, respectively.

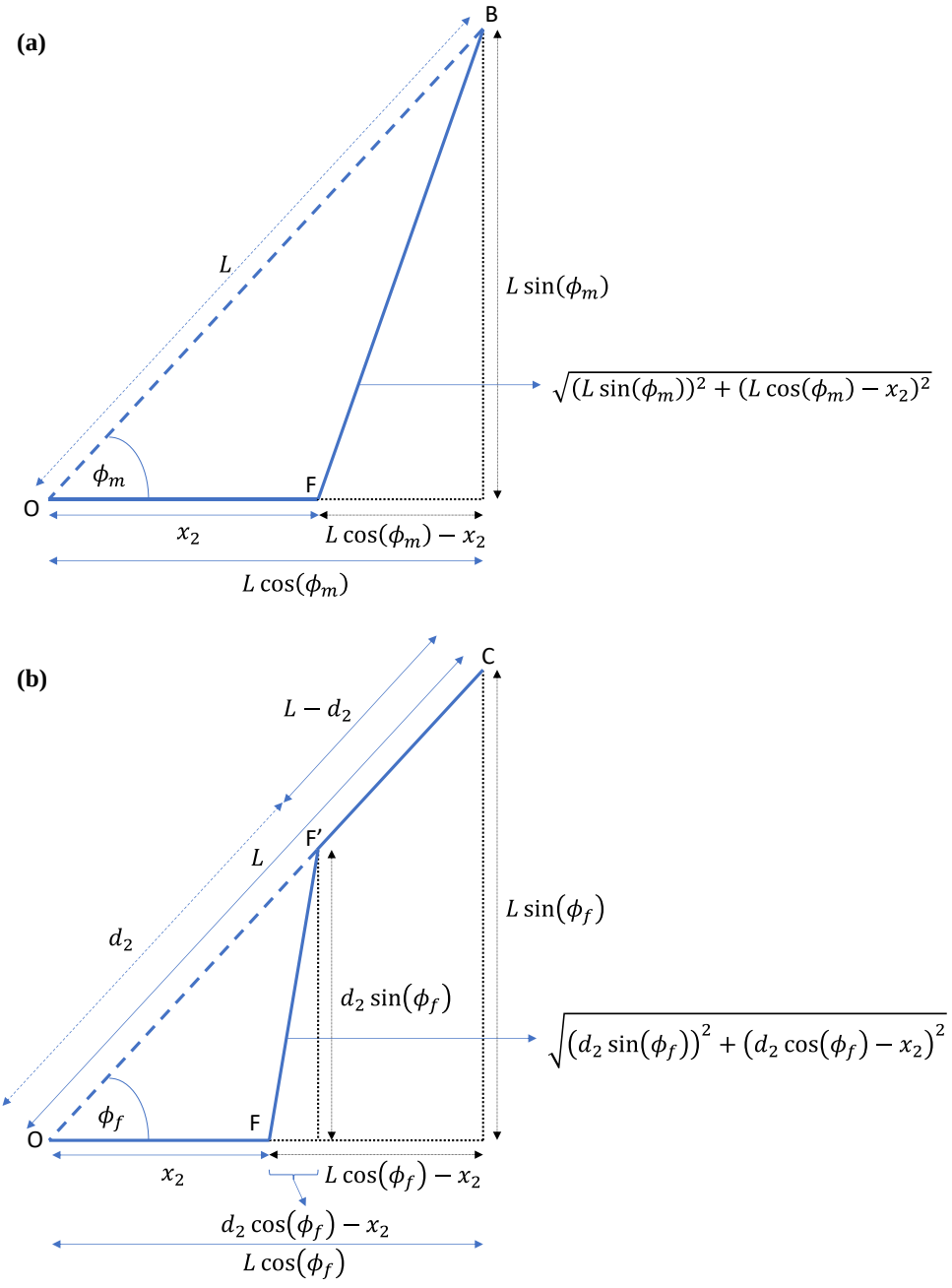

Figure 29. A schematic showing the geometrical relationships for the (a) mobile and (b) forest dislocation portions.

From these geometric representations in Figure 29, it can be deduced that the angles β_m and β_f for the mobile and forest dislocation portions, respectively, are

$$\beta_m = \tan\left(\frac{L\sin(\phi_m)}{L\cos(\phi_m) - x_2}\right) \quad \text{Eq. 31}$$

$$\beta_f = \tan\left(\frac{d_2\sin(\phi_f)}{d_2\cos(\phi_f) - x_2}\right) \quad \text{Eq. 32}$$

Now, the variable Q comes in play when determining the behavior of the system in the presence of solute along the forest dislocation CD is of interest. This variable only appears in the self-energy equation for dislocation segments CF' and DE' as

$$E_{CF'/DE'}(\alpha) = \int_{\Gamma} \{A(1 - \nu\cos^2(\alpha)) + Q\}\, ds \quad \text{Eq. 33}$$

Therefore, the potential energy of the entire system of dislocations is defined as

$$\begin{aligned} E^p_{Total} = {} & E^p_{AE}\left(x_1,\ \tau_m, \vec{b}_m\right) + E^p_{BF}\left(x_2,\ \tau_m, \vec{b}_m\right) + E^p_{EF}\left(x_1, x_2,\ \vec{b}_j\right) \\ & + E^p_{DE'}(Q, d_1) + E^p_{CF'}(Q, d_2) \\ & + E^p_{EE'}\left(x_1, d_1, \tau_f, \vec{b}_f\right) + E^p_{FF'}\left(x_2, d_2, \tau_f, \vec{b}_f\right) \end{aligned} \quad \text{Eq. 34}$$

Finally, formulation of the energy minimization problem is

$$\min_{x_1, x_2, d_1, d_2} \quad \left(E^p_{Total}\right)\Big|_{\vec{b}_m, \vec{b}_f, \tau_m, \tau_f, Q} \quad \text{Eq. 35}$$

It is noted that all parameters and variables in this problem can be normalized for convenience as shown in Table 4. The minimization procedure is performed by coding all the discussed relevant equations into MATLAB.

Table 4. Normalizations of the quantities used in the minimization problem.

Quantity	Normalization
E	$E^* = \frac{1}{AL}E$
W	$W^* = \frac{1}{AL}W$
Q	$Q^* = \frac{Q}{A}$
τ	$\tau^* = \frac{bL}{A}\tau$
x	$x^* = \frac{x}{L}$
d	$d^* = \frac{d}{L}$

5.1.3 Unzipping and dislocation instability

Before beginning the minimization of this problem, it is important to first understand when a solution has been achieved when the mobile dislocation is loaded. The critical stress ($\tau^*_{c_m}$) required for the mobile dislocation to break free from the Lomer-Cottrell lock is reached depending on two scenarios. First, case is unzipping, which occurs when the junction length goes to zero (i.e., $x_1 + x_2 \rightarrow 0$) as τ^*_m increases. Second, mobile dislocation instability (MDI) occurs when the solver fails to find a solution. Physically, this is equivalent to the bowing out mobile dislocation reaching the critical Frank-Read critical stress beyond which it becomes unstable and escapes [60,111].

Geometrically, MDI occurs when there is no ellipse with semiaxes $a_1 = r\mu b \ln\left(\frac{R}{r_0}\right)/4\pi\tau_m$ and $a_2 = a_1/r$ — per Eq. 25 — that can fit both end points of the bowing out mobile dislocation arm. This can also be extended to forest dislocation instability (FDI) in the same manner if the forest dislocation is loaded.

5.2 Results

5.2.1 Unloaded junction length orientation dependence

First, the isotropic line tension model was used to determine the variation of the Lomer-Cottrell lock stair rod length with respect to the dislocation orientations (symmetric cases — $\phi_m = \phi_f$). This is because it is important to check the validity of the derived model against what is reported in the literature for the simple isotropic case. This dependency is illustrated in Figure 30(a). To account for the dislocation direction dependence on these results, ν is taken to be 0.347, which is typical for Al [60,62]. As evident from this figure, the derived model in this work matches the results reported in literature exactly.

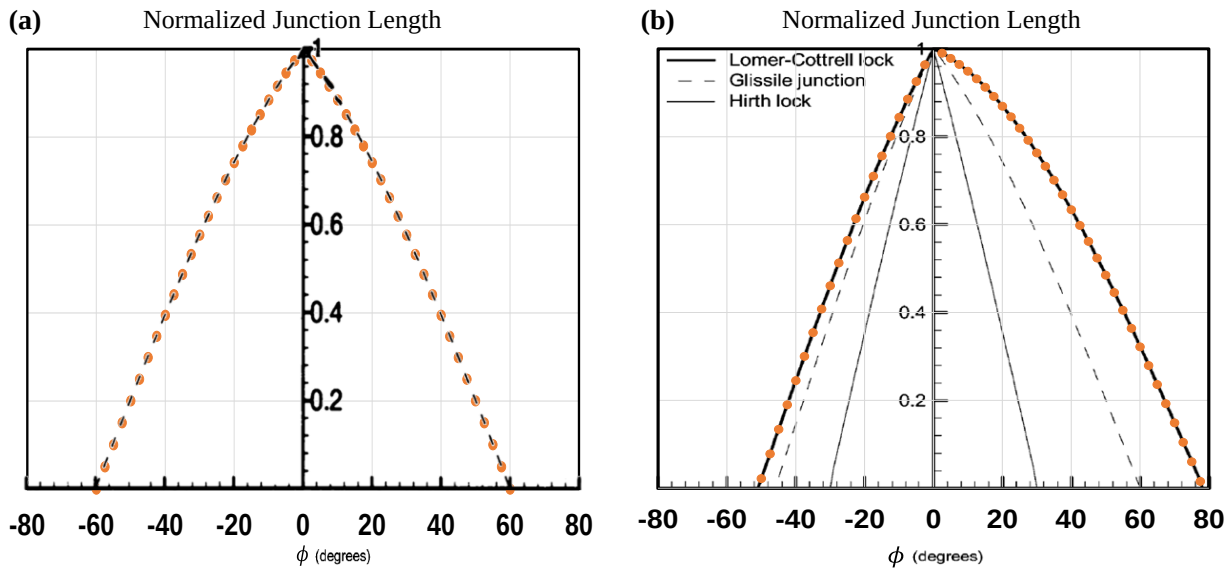

Figure 30. Normalized stair rod length dependence on the angle ϕ for symmetric Lomer-Cottrell lock cases using (a) the isotropic and (b) anisotropic line tension models. The filled orange circles represent the results from this current work. The dashed line in (a) represents the results as reported by Shenoy [62] while the thick solid and thin solid and dashed lines in (b) are reported by Dupuy and Fivel [60].

5.2.2 Unloaded junction length dependence on solute cluster size

The anisotropic line tension model was then used to predict the formation of the junction with respect to the amount of solute pinning the forest dislocation (i.e., dependence of the junction length on Q^*) for the unloaded case ($\tau_m^* = \tau_f^* = 0$). Figure 31 shows this dependency as well as that of the length of the initial forest dislocation configuration that has escaped to reach equilibrium. Since the case that is shown in the figure is for $\phi_m = \phi_f = 60°$ (i.e., symmetric), $x_1^* = x_2^* = x^*$ and $d_1^* = d_2^* = d^*$. It is observed from the figure that both x^* and d^* decrease as the binding energy increases in magnitude. Furthermore, the onset of the variation of both parameters does not ensue until reaching Q_1^*, and it ends after reaching Q_2^*.

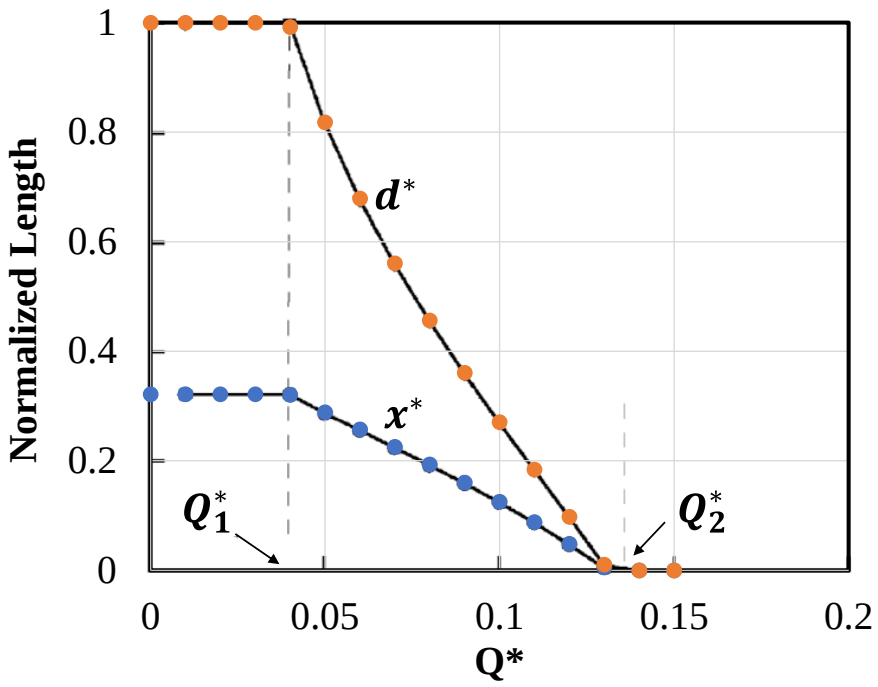

Figure 31. Symmetric ($\phi_m = \phi_f = 60°$) Lomer-Cottrell lock formed length (x^*) and unbound length of the forest dislocation from its solute cluster (d^*) variation with the binding energy of the forest dislocation to its solute cluster. The solid lines represent results as reported by Picu [111] while the blue and orange filled circles represent values of x^* and d^*, respectively, obtained in the current work.

5.2.3 Strength of junction dependence on solute cluster size

Now that the junction dependence on the binding energy has been verified against results in the literature, it is possible to go further and predict the value of $\tau_{c_m}^*$ required to escape the junction. In this case, no stress is applied on the forest dislocation ($\tau_f^* = 0$). First, the model is used both isotropically and anisotropically to determine the effect of considering dislocation directionality. Moreover, the effect of accounting for shape of the bowed-out dislocation is determined by setting it once as a circular arc ($a_1 = a_2$ in Eq. 26) and another as an elliptical arc ($r = 1.75$ [111] in Eq. 25). In all these mentioned cases, $\tau_{c_m}^*$ increases with more solute as shown

in Figure 32. The distinctions between these cases are also observed such that using the isotopic model results in the lowest values of $\tau_{c_m}^*$, and the critical stress plateau reaches a values of 1. This is opposed to taking the anisotropic approach (either circular or elliptical dislocation bow-out arc), which results in higher $\tau_{c_m}^*$ values. Figure 32 also shows that setting the dislocation bow-out shape as a circular arc results in relatively lower $\tau_{c_m}^*$ values than as an elliptical arc. The critical stress plateau for the circular is 1.3 and 1.43 for the elliptical arc shape.

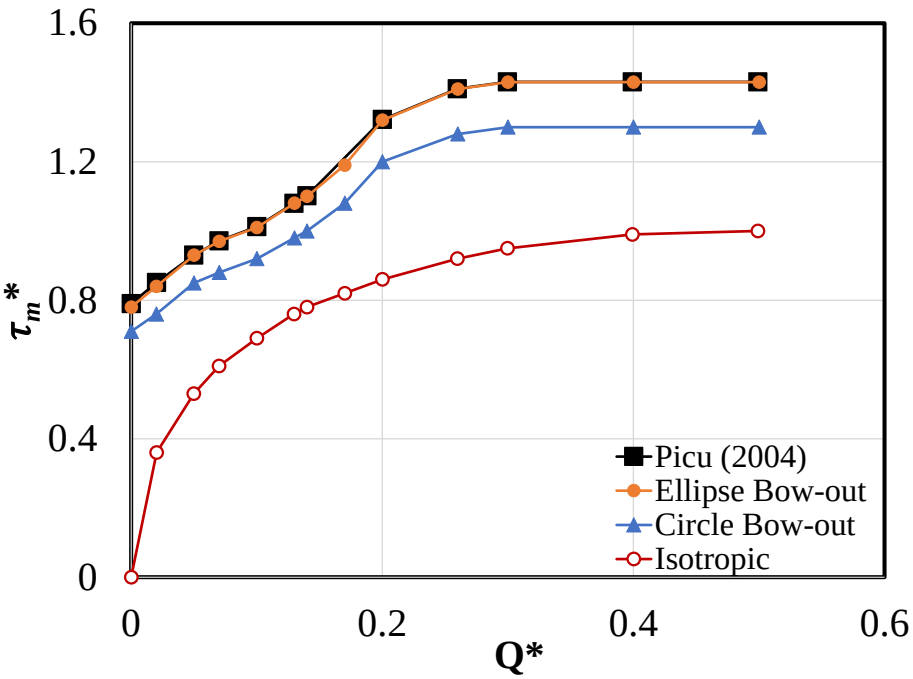

Figure 32. The strength of the Lomer-Cottrell lock dependence on the binding energy of the forest dislocation to its solute cluster for $\tau_f^* = 0$. This plot is for the symmetric ($\phi_m = \phi_f = 60°$) case. The filled orange circle are results from the current work attempting to reproduce the results of reported by Picu [111] using the anisotropic model (filled black squares) with an elliptical arc mobile dislocation bow-out. The filled blue triangles represent results generated using the direction dependent model with a circular arc mobile dislocation bow-out while the empty red circles are generated using the direction independent model.

5.3 Discussion

5.3.1 Unloaded state

To start with, the importance of accounting for the dislocation directionality is observed Figure 30 initially. This is because the isotropic approach fails to predict junction formation for $\phi < -60°$ and $\phi > 60°$ even though studies performed on this problem using nodal and atomistic simulations report junction formations for $-52° < \phi < 80°$, which are in agreement with the results of the anisotropic approach $-51° < \phi < 78°$ [60,45]. As expected, the shape of the variation of the junction length with the configurational angle ϕ is symmetric (i.e., same junction length whether ϕ is positive or negative). This is because the sign of ϕ does not matter in the isotropic case as no sense of dislocation directionality is incorporated. On the other hand, accounting for that directionality results in a slightly asymmetric plot for the junction length against ϕ; another point underlining the importance of considering the dislocation direction. Keeping in mind the domain at which junction formation occurs, it is deduced that using the isotropic model would not show any variation of x^* or d^* ($x^* = d^* = 0$) with respect to the Q^* if dislocation directionality is not accounted for. This is in contrast to the results when taking the anisotropic approach as seen in Figure 31.

As mentioned in Section 4.2.2, the effect of the solute clusters along the forest dislocation does not seem to take effect on either x^* or d^* until reaching some value Q_1^*, and they both remain at zero (i.e., the dislocations are at a crossed state) beyond another value Q_2^*. These two values are specific to each configurational case that is investigated in this problem; different ϕ values would result in other distinct values of Q_1^* and Q_2^*. For instance, at $\phi = 60°$, $Q_1^* = 0.04$ and $Q_2^* = 0.13$ (Figure 31) while at $\phi = 20°$, $Q_1^* = 0.28$ and $Q_2^* = 0.64$ (Figure 33).

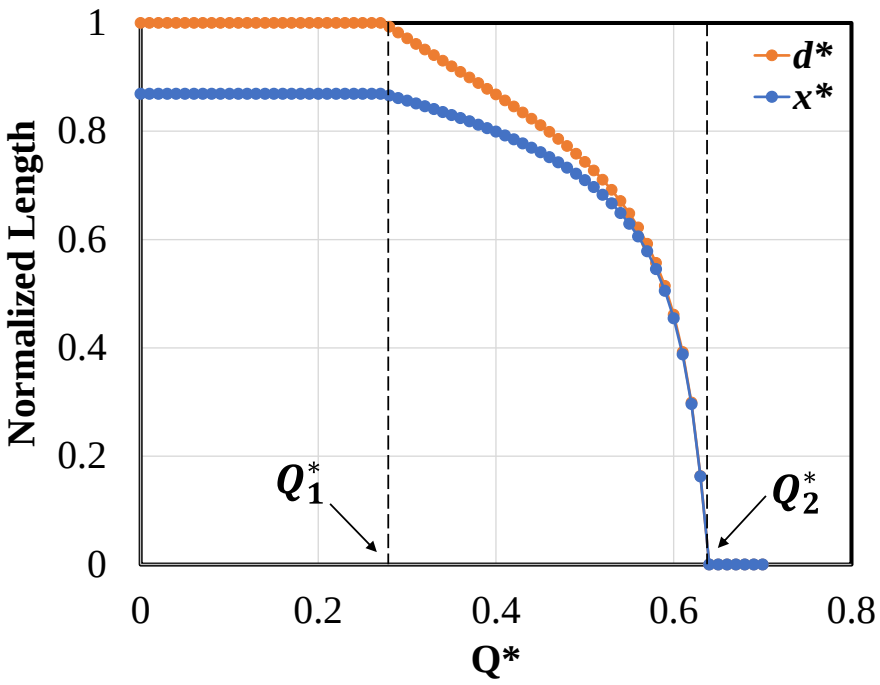

Figure 33. The dependency of x^* and d^* on the binding energy for a Lomer-Cottrell lock with an initial configuration of $\phi_m = \phi_f = 20°$.

5.3.2 Loaded state

The results in Figure 32 show that the junction strength is much weaker when ignoring the anisotropy of the dislocation. In this case, the figure shows an expected result of $\tau_{c_m}^* = 0$ for $Q^* = 0$. This is because there is no junction formation using this approach for the case of $\phi_m = \phi_f = 60°$ as discussed in Section 4.3.1. This means that upon applying an infinitesimal quantity of τ_m^*, the mobile dislocation readily escapes. However, this does not agree with results reported using nodal and atomistic simulations [62-65]. This emphasizes the importance of accounting for the direction dependence of dislocations using the line tension model.

Another major point to take away from the results is that dislocation bow-out shape matters if precise breakaway stress values are desired. This is due to the difference between the values as well as the similarity in the trend of the evolution of the junction strength with the amount of solute. Additionally, it is noted that the two modes of failure of the junction discussed in Section 4.1.2 can be observed from Figure 31 and Figure 32. More specifically, the mobile dislocation escapes the junction by unzipping in all computed critical stresses $\tau_{c_m}^*$ for $Q^* < Q_2^*$. For $Q^* > Q_2^*$, the mode of failure is MDI. $\tau_{c_m}^*$ then reaches a stress plateau after reaching the solute saturation limit at Q_S^*, which is equal to 0.3 in the symmetric case of $\phi_m = \phi_f = 60°$. This stress plateau is referred to as the saturation stress ($\tau_{s_m}^*$). Despite the observed behavior in Figure 32 that changing the dislocation bow-out shape affects $\tau_{s_m}^*$, it appears that it does not have much influence on Q_S^*.

5.3.3 Understanding the relation to DSA

Now that the junction strength relationship to solute cluster size has been determined, it is possible to be place this line tension model as an opening door to the path of further understanding DSA in both FCC and HCP alloys. It is important to note that this model defines the forest dislocation as the one that is slow enough for solute clusters to form upon. The time it takes for the solute to form along the forest dislocation called the forest aging time t_a. On the other hand, the mobile dislocation is the one that is fast enough that no solute has a chance to diffuse toward it to form a cluster or atmosphere. Thus, the associated waiting time (t_w) for a mobile dislocation before it escapes the junction is comparatively smaller than t_a, so the forest dislocation takes precedence for the solute diffusion.

To understand how this figures into DSA phenomenologically, it is useful to grasp the notion that for longer t_a (i.e., lowering the strain rate), more solute diffuse toward the forest dislocation (i.e., Q^* increases). As discussed in Section 4.3.3 (also evident from Figure 32), more solute means more binding energy which in turn means increasing junction strength for $Q^* \leq Q_S^*$. In short, lowering the strain rate results in an increase in strength (definition of the negative strain rate sensitivity), and this is how the line tension model can play a role in DSA. What needs to be added to it is another model that captures t_a, t_w, and Q_S^*.

Indeed, the negative strain rate sensitivity model was developed by Picu [111] by implementing an average shear stress acting on the mobile plane (determined with t_a, t_w, and Q_S^*) arising from the stress required for a mobile dislocation to escape a population of junctions. Per Eq. 5, the strain rate is still required to compute the SRS. In fact, by the definition of mobile dislocation average waiting time, it is related to $\dot{\varepsilon}_p$ by

$$t_w = \Omega/\dot{\varepsilon}_p \qquad \text{Eq. 36}$$

where Ω is a characteristic strain determined by Kubin and Estrin [115] to be about 3×10^{-3} and is defined by the mobile and forest dislocation densities (ρ_m and ρ_f, respectively) as

$$\Omega = \frac{\rho_m b}{\sqrt{\rho_f}} \qquad \text{Eq. 37}$$

Additionally, Picu accounted only for the pinned forest dislocations as obstacles to the dislocation. A few years later, this model was further built upon by Soare and Curtin [53,54] to

include the contribution of the friction stress, solute strengthening, and strength associated with the aging of the mobile dislocation.

5.3.4 Extension to HCP Mg

Now that the line tension modelling approach has been laid out in great detail, it is safe to say that the application of this model may be extended toward Basal/Prismatic type <a> dislocation interactions in HCP. This is of great importance as it was shown by Stricker and Weygand [61], who performed DDD simulations on dislocation-dislocation interactions in FCC crystal structures, that although Lomer-Cottrell locks occur during plastic strain, the occurrence of glissile junction formations and collinear annihilation interactions are more common during plastic deformation and have an overall effect on the dislocation density and strength of the material. They also found that interactions leading to Hirth lock formations are much less compared to the other interactions, and thus they concluded that glissile junction formations and collinear annihilation interactions exhibit the highest contribution to the dislocation density and strength of the material.

However, it is noted here that not all types of junction formation in FCC alloys are relevant to HCP; namely, the Lomer-Cottrell and Hirth locks. Rather, the only types resulting from Basal/Prismatic <a> interactions are the collinear annihilation and glissile junction. This means that the importance of these two cases should be explored further for HCP Mg within the framework of DSA due to their impact on dislocation density and strength (which are important factors of DSA as discussed in Section 2.8) and the only relevance in Basal/Prismatic <a> interactions. In this section, the path toward achieving such destination is provided for future work.

Before discussing the differences between the two HCP dislocation-dislocation interactions, it is advised that the cases are drawn schematically just like it is shown in Section 4.1 to better relate the work performed on FCC to HCP. In this work, the two-dimensional (2-D) representations of the collinear annihilation and glissile junction formation are provided in Figure 34 and Figure 35, respectively. Additionally, it is encouraged to draw a 3-D schematic in order to have a good sense and view of the directionality of the dislocations in the problem and to determine the important angle relationships (as discussed in Section 4.1.1).

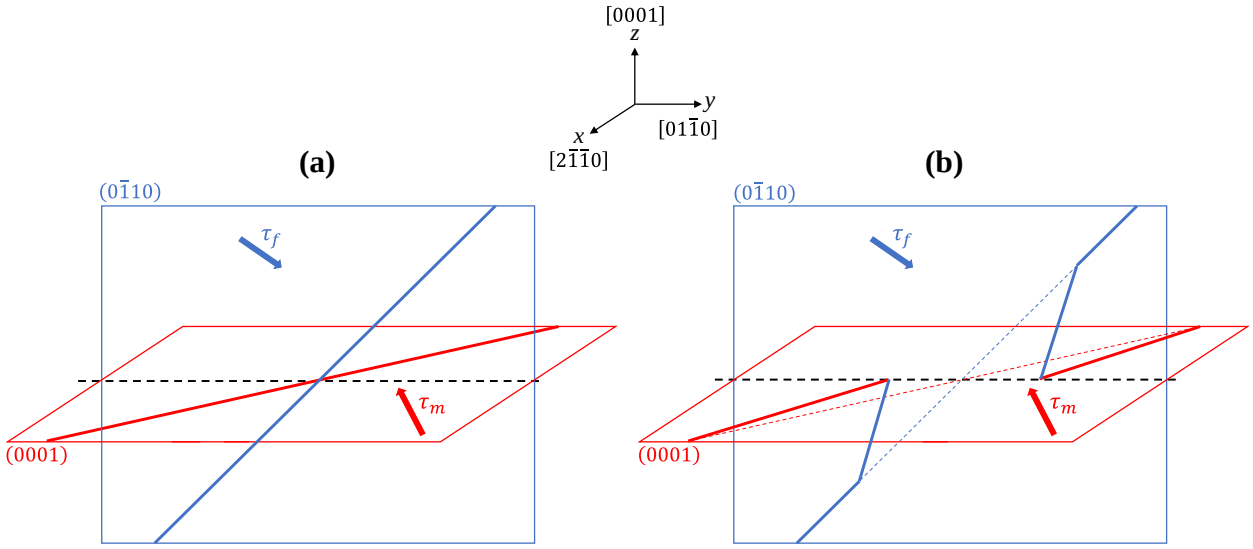

Figure 34. A 2-D schematic of the collinear annihilation interaction in HCP crystals. The red and blue lines represent the mobile and forest dislocations, respectively.

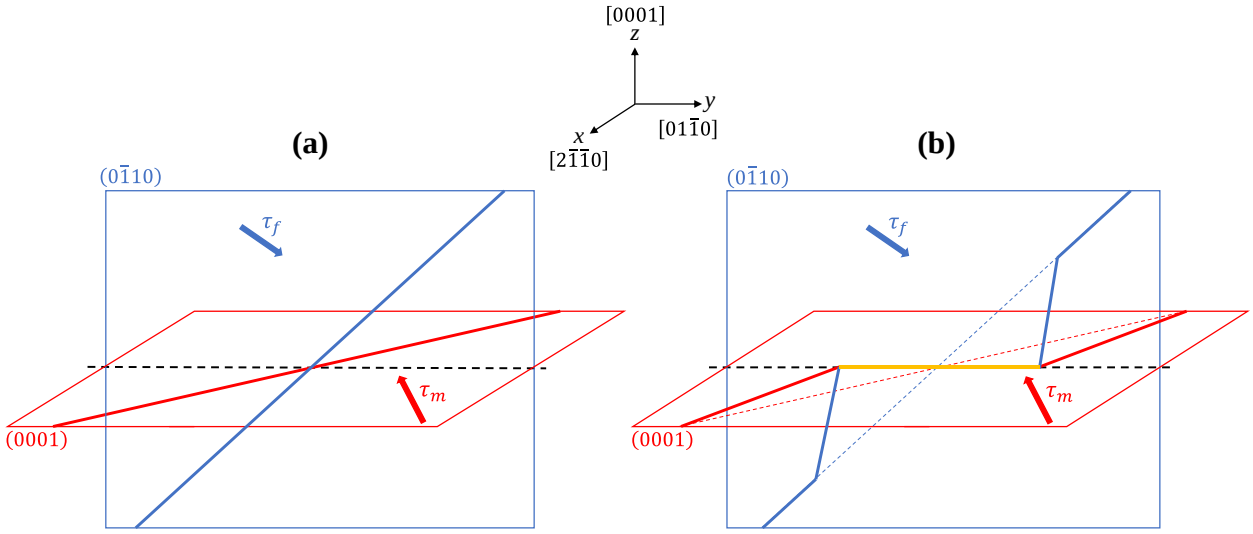

Figure 35. A 2-D schematic of the glissile junction formation in HCP crystals. The red and blue lines represent the mobile and forest dislocations, respectively.

In Figure 34, the mobile dislocation has a Burgers vectors $\vec{b}_m$ of $\frac{1}{3}[\bar{1}2\bar{1}0]$ and lies in the (0001) basal slip plane while the forest dislocation has a Burgers vectors $\vec{b}_f$ of $\frac{1}{3}[1\bar{2}10]$ and lies in the $(0\bar{1}10)$ prism slip plane. Therefore, the resulting $\vec{b}_j$ equals to zero, leading to no junction formation with the mobile and forest dislocation arms attached to one another on each side of the interaction; this is the major observable distinction from Lomer-Cottrell lock formation. This means that the junction corresponding to line EF in the Lomer-Cottrell lock case (Figure 25) does not exist physically in the model, and thus has no potential energy contribution (E_{EF}^{p}). This does not change the total potential energy equation (Eq. 34), however, other than removing E_{EF}^{p}. (i.e., the geometric derivations remain unchanged). In this sense, the length $x_1 + x_2$ would not mean the formed junction length; rather, it would be the separation distance between the two encountering points connecting the arms of the two dislocations. This distinction also leads to the irrelevance of the term of "*unzipping*" of a junction in the HCP case; rather, it would be better to call it as "*postseparation encounter*," which is still governed by the same condition that $x_1 + x_2 \rightarrow$

0. The mobile dislocation escape mode via MDI is also still applicable in the same manner as discussed in Section 4.1.2.

In Figure 35, the mobile dislocation has a Burgers vectors $\vec{b}_m$ of $\frac{1}{3}[\bar{1}2\bar{1}0]$ and lies in the (0001) basal slip plane while the forest dislocation has a Burgers vectors $\vec{b}_f$ of $\frac{1}{3}[2\bar{1}\bar{1}0]$ and lies in the $(0\bar{1}10)$ prism slip plane. Therefore, the resulting $\vec{b}_j$ is $\frac{1}{3}[11\bar{2}0]$. This means that the formed junction is glissile (i.e., able to glide in the slip plane) because it lies in a favor slip plane — the (0001) basal plane. This is what makes it different from the Lomer-Cottrell lock, which is a sessile junction (i.e., its Burgers vector does not lie in a favorable slip plane). In other words, the glissile junction dislocation bow-out must be accounted for because it lies in the same plane that the has an applied τ_m. Other than that, it would seem that following the line tension model would still be similar to the FCC Lomer-Cottrell lock case.

5.4 Conclusions

1. It is important to take dislocation character dependence into consideration when using the line tension model. Ignoring dislocation character leads to underprediction of the junction lengths (and hence, strengths), as revealed by comparison with more sophisticated modeling approaches, such as discrete dislocation dynamics and those informed by atomistic calculations. Given the high importance of dislocation character in the results of the calculations, careful initial problem setup is emphasized because, not only are the relative orientations of the Burgers vectors of the dislocations important, but their line directions also figure prominently in the final results.

2. As a corollary to the above conclusion, line tension anisotropy also influences the shape of bowed out (stressed) dislocations as well as straight segments. Accounting for the near elliptical bow out shape (rather than circular) is also important to avoid underestimation of the stress required for a mobile dislocation to escape the junction.

3. The escape of the mobile dislocation was explored by ascribing a binding energy to the forest dislocation (i.e., presence of pinning solute) which inhibits junction formation. The result originally obtained by Picu in his landmark paper was reproduced; more solute means more binding energy, which in turn means increasing junction strength for binding energies below the saturation limit. This serves to be the fundamental unit process which is responsible for negative strain rate sensitivity (DSA). Slower strain rates permit the forest dislocations to be more highly pinned and the resulting junctions to be more difficult to escape. Notably, this overall result is insensitive to the aforementioned details of dislocation bow-out shape.

4. It is possible to extend the application of the line tension model to HCP Mg while keeping in mind its distinctions from FCC alloys. The application of this model as a step toward DSA is of importance because it has been observed experimentally in many Mg alloys. This is because the role of forest dislocations and junction formations have to be accounted for in order to capture a negative strain rate sensitivity.

Chapter 6: Conclusions and Future Work

In summary, this work has investigated the applicability of the principle of "stress equivalence" and used the Leyson-Curtin static solute strengthening theoretical model as a guide to derive a purely experimental input-based model to predict the flow stress dependence on temperature and strain rate in the low temperature regime. Future work can include further investigation of strain rate jump test data at temperatures and strain rates where DSA is active.

Furthermore, the work laid out a detailed procedure of the exact methodology to use the line tension model through the energy minimization approach. All of this procedure is explained in great detail in an attempt to fill a gap in the literature by connecting previous junction formation studies into one place and illustrate the details that are not explained clearly in the literature. Lastly, one should take the work of Picu [111] and expand its application into other dislocation-dislocation interaction cases in FCC alloys (Hirth locks, glissile junctions, and collinear annihilation) as well as other interaction cases that are only relevant to HCP Mg (glissile junctions and collinear annihilation).

The following is a summary of all conclusions deduced from this work:

(1) EVPSC (elasto-viscoplastic self-consistent) polycrystal plasticity simulations indicate that the dominant slip mode during tensile microyielding of these textured polycrystalline Mg alloys is basal slip. However, non-basal mechanisms (especially prismatic slip) are activated during macroyielding. Correspondingly, the *effective* Taylor factor very quickly approaches a value which remains rather constant throughout the tensile test.

(2) The EVPSC results also indicate that the steady-state change in relative slip activity during strain rate jump tests is small for the rate jump magnitudes typically enforced experimentally. That is, the relative slip activities quickly return to values close to the original magnitude after a transient response associated with the strain rate change.

(3) EVPSC polycrystal plasticity simulations for repeated stress relaxation tests indicate that the change in relative slip activity is significant and does not return to the original magnitude. Thus, caution should be exercised when interpreting the results of stress relaxation tests performed on materials that deform by multiple mechanisms at once.

(4) The experimental results show that the generalized Cottrell-Stokes law (the strain rate sensitivity is insensitive to strain hardening) holds for textured, polycrystalline, binary Mg alloys deformed in tension. It is hypothesized that the rate controlling mechanism is related to basal-prismatic forest dislocation interactions, regardless of which mode dominates strain accommodation.

(5) The principle of "stress equivalency" originally introduced in the context of oriented single crystals is shown to also hold for tensile deformation of basal textured polycrystalline Mg alloys. Notably, this conclusion is insensitive to the choice of Taylor factor because the slope of the Basinski plot is close to unity over the range of interest. This means that changing the Taylor factor would only result in shifting the data points together along the same straight line; meaning that the stress equivalence principle still holds for different Taylor factors.

(6) This means that once the yield strength of an alloy at a low temperature is known, the activation volume at yield can be directly predicted. With this activation volume, the

flow stress can be predicted at any other temperature or strain rate, provided one employs the appropriate model for the rate and temperature regime of interest.

(7) It is important to take dislocation character dependence into consideration when using the line tension model. Ignoring dislocation character leads to underprediction of the junction lengths (and hence, strengths), as revealed by comparison with more sophisticated modeling approaches, such as discrete dislocation dynamics and those informed by atomistic calculations. Given the high importance of dislocation character in the results of the calculations, careful initial problem setup is emphasized because, not only are the relative orientations of the Burgers vectors of the dislocations important, but their line directions also figure prominently in the final results.

(8) As a corollary to the above conclusion, line tension anisotropy also influences the shape of bowed out (stressed) dislocations as well as straight segments. Accounting for the near elliptical bow out shape (rather than circular) is also important to avoid underestimation of the stress required for a mobile dislocation to escape the junction.

(9) The escape of the mobile dislocation was explored by ascribing a binding energy to the forest dislocation (i.e., presence of pinning solute) which inhibits junction formation. The result originally obtained by Picu in his landmark paper was reproduced; more solute means more binding energy, which in turn means increasing junction strength for binding energies below the saturation limit. This serves to be the fundamental unit process which is responsible for negative strain rate sensitivity (DSA). Slower strain rates permit the forest dislocations to be more highly pinned and the resulting junctions

to be more difficult to escape. Notably, this overall result is insensitive to the aforementioned details of dislocation bow-out shape.

(10) It is possible to extend the application of the line tension model to HCP Mg while keeping in mind its distinctions from FCC alloys. The application of this model as a step toward DSA is of importance because it has been observed experimentally in many Mg alloys. This is because the role of forest dislocations and junction formations have to be accounted for in order to capture a negative strain rate sensitivity.

References

[1] McCosh, D. (1994). Emerging Technologies for the Supercar. *Popular Science, 244*(6), 95-100.

[2] Sissine, F. (1996). The partnership for a new generation of vehicles (PNGV).

[3] Eisenstein, P. A. (1994). Supercar director defends program. *The Washington Times*, E1.

[4] Fuhs, A. (2008). *Hybrid vehicles: and the future of personal transportation*. CRC press.

[5] Türk, H. (2014). The oil crisis of 1973 as a challenge to multilateral energy cooperation among Western industrialized countries. *Historical Social Research/Historische Sozialforschung*, 209-230.

[6] Agreement, P. (2015, December). Paris agreement. In *Report of the Conference of the Parties to the United Nations Framework Convention on Climate Change (21st Session, 2015: Paris). Retrived December* (Vol. 4, p. 2017). HeinOnline.

[7] Falkner, R. (2016). The Paris Agreement and the new logic of international climate politics. *International Affairs*, *92*(5), 1107-1125.

[8] Zhu, S. M., & Nie, J. F. (2004). Serrated flow and tensile properties of a Mg–Y–Nd alloy. *Scripta Materialia*, *50*(1), 51-55.

[9] Chávez, B., Garcés, G., Pérez Zubiaur, P., Barea, R., & Adeva, P. (2020). Dynamic Strain Aging (DSA) in solid solubilized Mg-Gd alloys under compression at intermediate temperatures. *Revista De Metalurgia*, *56*(3), e175.

[10] Liao, J., Liu, J., Zhang, L., & Xue, X. (2020). Influence of heating mode on orange peel patterns in warm incremental forming of magnesium alloy. *Procedia Manufacturing*, *50*, 5-10.

[11] Nakanishi, E., Tateno, H., Hishida, Y., & Shibata, K. (1998). New materials technology for achieving both crashworthiness and weight reduction using energy-absorbing steel with higher strain-rate sensitivity. *SAE transactions*, 680-686.

[12] Sun, S., & Xue, Z. (2021). Effect of Aging Process on the Strain Rate Sensitivity in V-Containing TWIP Steel. *Metals*, *11*(1), 126.

[13] Sills, R. B., & Cai, W. (2016). Solute drag on perfect and extended dislocations. *Philosophical Magazine*, *96*(10), 895-921.

[14] Fleischer, L., Hibbard, W. (1963). In "The Relation Between the Structure and Mechanical Properties of Metals." *Proceedings of the National Physical Laboratory. Metallurgy Division. HM Stationery Office*, London, 261.

[15] Friedel, J. (1964). *Dislocations*. Addison-Wesley. *New York*, 224.

[16] Akhtar, A., & Teghtsoonian, E. (1969). Solid solution strengthening of magnesium single crystals—I alloying behaviour in basal slip. *Acta Metallurgica*, 17(11), 1339-1349.

[17] Labusch, R. (1970). A statistical theory of solid solution hardening. *physica status solidi (b)*, 41(2), 659-669.

[18] Labusch, R. (1972). Statistische theorien der mischkristallhärtung. *Acta Metallurgica*, *20*(7), 917-927.

[19] Argon, A. (2007). Solid-solution Strengthening, In *Strengthening Mechanisms in Crystal Plasticity* (vol. 4 pp. 136-191). Oxford University Press on Demand.

[20] Tehranchi, A., Yin, B., & Curtin, W. A. (2018). Solute strengthening of basal slip in Mg alloys. *Acta Materialia*, *151*, 56-66.

[21] Mohanty, G., Wheeler, J. M., Raghavan, R., Wehrs, J., Hasegawa, M., Mischler, S., ... & Michler, J. (2015). Elevated temperature, strain rate jump microcompression of nanocrystalline nickel. *Philosophical Magazine*, 95(16-18), 1878-1895.

[22] Basinski, Z. S., Jackson, P. J., & Duesbery, M. S. (1977). Transients in steady-state plastic deformation produced by changes of strain rate. *Philosophical Magazine*, *36*(2), 255-263.

[23] Wagoner, R. H. (1984). Strain-rate sensitivity of zinc sheet. *Metallurgical and Materials Transactions A*, *15*(6), 1265-1271.

[24] Caillard, D., & Martin, J. (2003). Experimental characterization of dislocation mechanisms. *Thermally activated mechanisms in crystal plasticity*, *Pergamon Materials Series, Elsevier Science, Cambridge, UK*, 15-18.

[25] Cottrell, A. H., & Stokes, R. J. (1955). Effects of temperature on the plastic properties of aluminium crystals. *Proceedings of the Royal Society of London. Series A. Mathematical and Physical Sciences*, *233*(1192), 17-34.

[26] Haasen, P. (1958). Plastic deformation of nickel single crystals at low temperatures. *Philosophical Magazine*, *3*(28), 384-418.

[27] Nabarro, F. R. N. (1990). Cottrell-Stokes law and activation theory. *Acta Metallurgica et Materialia*, *38*(2), 161-164.

[28] Kocks, U. F., & Chen, S. R. (1992). On the two distinct effects of thermal activation on plasticity: application to nickel. *Physica status solidi (a)*, 131(2), 403-413.

[29] Mulford, R. A., & Kocks, U. F. (1979). New observations on the mechanisms of dynamic strain aging and of jerky flow. *Acta Metallurgica*, *27*(7), 1125-1134.

[30] Basinski, Z. S., Foxall, R. A., & Pascual, R. (1972). Stress equivalence of solution hardening. *Scripta Metallurgica*, *6*(9), 807-814.

[31] Nabarro, F. R. N. (1985). Thermally activated dislocation glide in moderately concentrated solid solutions. *Philosophical Magazine B*, *52*(3), 785-793.

[32] Labusch, R. (1970). A statistical theory of solid solution hardening. *physica status solidi (b)*, 41(2), 659-669.

[33] Labusch, R. (1972). Statistische theorien der mischkristallhärtung. *Acta Metallurgica*, *20*(7), 917-927.

[34] Nabarro, F. (1985). In "Dislocations and Properties of Real Materials." *Institute of Metals*, London, 152.

[35] Leyson, G. P. M., & Curtin, W. A. (2016). Solute strengthening at high temperatures. *Modelling and Simulation in Materials Science and Engineering*, *24*(6), 065005.

[36] Leyson, G. P. M., & Curtin, W. A. (2016). Thermally-activated flow in nominally binary Al–Mg alloys. *Scripta Materialia, 111*, 85-88.

[37] Leyson, G. P. M., Hector Jr, L. G., & Curtin, W. A. (2012). Solute strengthening from first principles and application to aluminum alloys. *Acta Materialia*, *60*(9), 3873-3884.

[38] Leyson, G. P. M., Hector Jr, L. G., & Curtin, W. A. (2012). First-principles prediction of yield stress for basal slip in Mg–Al alloys. *Acta materialia*, *60*(13-14), 5197-5203.

[39] Tehranchi, A., Yin, B., & Curtin, W. A. (2018). Solute strengthening of basal slip in Mg alloys. *Acta Materialia*, *151*, 56-66.

[40] C.H. Cáceres & P. Lukáč (2008) Strain hardening behaviour and the Taylor factor of pure magnesium, Philosophical Magazine, 88:7, 977-989.

[41] U.F. Kocks, C.N. Tomé, H.-R. Wenk, Texture and anisotropy: preferred orientations in polycrystals and their effect on materials properties, Cambridge university press, 2000.

[42] Miura, S., Imagawa, S., Toyoda, T., Ohkubo, K., & Mohri, T. (2008). Effect of rare-earth elements Y and Dy on the deformation behavior of Mg alloy single crystals. *Materials Transactions*, 0804070382-0804070382.

[43] Palosaari, M., & Manninen, T. (2012). Bake-Hardening of Stabilized Ferritic Stainless Steels. *Steel Research International*, Wiley-VCH Verlag GmbH, 951-954.

[44] Cottrell, A. H., & Bilby, B. A. (1949). Dislocation theory of yielding and strain ageing of iron. *Proceedings of the Physical Society*. Section A, 62(1), 49.

[45] Hosford, W. (2012). Strain Aging. In *Iron and Steel* (pp. 104-112). Cambridge: Cambridge University Press.

[46] Epperly, E. N., & Sills, R. B. (2020). Comparison of continuum and cross-core theories of dynamic strain aging. *Journal of the Mechanics and Physics of Solids*, 141, 103944.

[47] Ma, X., Li, F., Cao, J., Li, J., Sun, Z., Zhu, G., & Zhou, S. (2018). Strain rate effects on tensile deformation behaviors of Ti-10V-2Fe-3Al alloy undergoing stress-induced martensitic transformation. *Materials Science and Engineering: A*, *710*, 1-9.

[48] Han, Z., Ding, C., Liu, G., Wei, R., & Zhang, G. (2021). Dynamic precipitation-induced the negative strain rates sensitivity in VCoNi medium-entropy alloy. *Materials Letters*, *290*, 129480.

[49] Chen, H., Chen, Z., Ji, G., Zhong, S., Wang, H., Borbély, A., ... & Bréchet, Y. (2021). The influence of shearable and nonshearable precipitates on the Portevin-Le Chatelier behavior in precipitation hardening AlMgScZr alloys. *International Journal of Plasticity*, *147*, 103120.

[50] Chun, Y. B., & Davies, C. H. J. (2011). Twinning-induced negative strain rate sensitivity in wrought Mg alloy AZ31. *Materials Science and Engineering: A*, *528*(18), 5713-5722.

[51] Curtin, W. A., Olmsted, D. L., & Hector, L. G. (2006). A predictive mechanism for dynamic strain ageing in aluminium–magnesium alloys. *Nature materials*, *5*(11), 875-880.

[52] Picu, R. C., & Zhang, D. (2004). Atomistic study of pipe diffusion in Al–Mg alloys. *Acta materialia*, *52*(1), 161-171.

[53] Soare, M. A., & Curtin, W. A. (2008). Solute strengthening of both mobile and forest dislocations: The origin of dynamic strain aging in fcc metals. *Acta Materialia*, *56*(15), 4046-4061.

[54] Soare, M. A., & Curtin, W. A. (2008). Single-mechanism rate theory for dynamic strain aging in fcc metals. *Acta Materialia*, *56*(15), 4091-4101.

[55] Rodriguez, P. (1984). Serrated plastic flow. *Bulletin of Materials Science*, 6(4), 653-663.

[56] Ait-Amokhtar, H., Fressengeas, C., & Bouabdallah, K. (2015). On the effects of the Mg content on the critical strain for the jerky flow of Al–Mg alloys. *Materials Science and Engineering: A*, *631*, 209-213.

[57] Bacon, D. J., Barnett, D. M., & Scattergood, R. O. (1980). Anisotropic continuum theory of lattice defects. *Progress in Materials Science*, 23, 51-262.

[58] Foreman, A. J. E. (1967). The bowing of a dislocation segment. Philosophical magazine, 15(137), 1011-1021.

[59] Wickham, L. K., Schwarz, K. W., & Stölken, J. S. (1999). Rules for forest interactions between dislocations. *Physical review letters*, 83(22), 4574.

[60] Dupuy, L., & Fivel, M. C. (2002). A study of dislocation junctions in FCC metals by an orientation dependent line tension model. *Acta Materialia*, 50(19), 4873-4885.

[61] Stricker, M., & Weygand, D. (2015). Dislocation multiplication mechanisms–Glissile junctions and their role on the plastic deformation at the microscale. *Acta Materialia*, 99, 130-139.

[62] Shenoy, V. B., Kukta, R. V., & Phillips, R. (2000). Mesoscopic analysis of structure and strength of dislocation junctions in fcc metals. *Physical Review Letters*, *84*(7), 1491.

[63] Zhou, S. J., Preston, D. L., Lomdahl, P. S., & Beazley, D. M. (1998). Large-scale molecular dynamics simulations of dislocation intersection in copper. *Science*, *279*(5356), 1525-1527.

[64] Bulatov, V., Abraham, F. F., Kubin, L., Devincre, B., & Yip, S. (1998). Connecting atomistic and mesoscale simulations of crystal plasticity. *Nature, 391*(6668), 669-672.

[65] Rodney, D., & Phillips, R. (1999). Structure and strength of dislocation junctions: An atomic level analysis. *Physical Review Letters*, *82*(8), 1704.

[66] Saada, G. (1960). Sur le durcissement dû à la recombinaison des dislocations. *Acta Metallurgica*, *8*(12), 841-847.

[67] Shabana, M. A., Bhattacharyya, J. J., Niewczas, M., & Agnew, S. R. (2021). Exploring stress equivalence for solid solution strengthened Mg alloy polycrystals. *Materials Science and Engineering: A*, 816, 141252.

[68] Akhtar, A., & Teghtsoonian, E. J. P. M. (1972). Substitutional solution hardening of magnesium single crystals. *Philosophical Magazine*, *25*(4), 897-916.

[69] Scharf, H., Lukáč, P., Boček, M., Haasen, P. (1968). Dependence of folw stress of magnesium-cadmium single crystals on concentration and temperature. *Z. Metallk*, 59, 799.

[70] Urakami, A., Meshii, M., Fine, M. (1970). Second International Conf. on the Strength of Metals and Alloys, Pacific Grove, California, *The American Society for Metals*, 272.

[71] Sheeley, W., Levine, E., Nash, R. (1959). *Trans. Am. Inst. Min. Engrs.*, 215, 693.

[72] Ogawa, Y., Ando, D., Sutou, Y., & Koike, J. (2016). Age-Hardening of Dual Phase Mg-Sc Alloy at 573 K. In *Magnesium Technology 2016* (pp. 147-149). Springer, Cham.

[73] Yamagishi, K., Ando, D., Sutou, Y., & Ogawa, Y. (2020). Texture Formation through Thermomechanical Treatment and Its Effect on Superelasticity in Mg–Sc Shape Memory Alloy. *Materials Transactions*, MT-M2020244.

[74] Mordike, B. L., & von Buch, F. (2000). Development of high temperature creep resistant alloys. *Magnesium Alloys and their Applications*, 35-40.

[75] Unsworth, W. (1989). The role of rare earth elements in the development of magnesium base alloys. *International journal of materials and product technology*, *4*(4), 359-378.

[76] Silva, C. J., Kula, A., Mishra, R. K., & Niewczas, M. (2018). The effect of Sc on plastic deformation of Mg–Sc binary alloys under tension. *Journal of Alloys and Compounds*, *761*, 58-70.

[77] Catherine J. Silva. (2014). Effect of Sc Addition on the Mechanical Properties of Mg-Sc Binary Alloys. M.S. thesis, McMaster University.

[78] Kula, A., Jia, X., Mishra, R. K., & Niewczas, M. (2017). Flow stress and work hardening of Mg-Y alloys. *International Journal of Plasticity*, *92*, 96-121.

[79] Jia, X. (2013). Solid solution strengthening and texture evolution in Mg-Y alloys. M.S. thesis, McMaster University.

[80] Basinski, Z. S., Jackson, P. J., & Duesbery, M. S. (1977). Transients in steady-state plastic deformation produced by changes of strain rate. *Philosophical Magazine*, *36*(2), 255-263.

[81] Wagoner, R. H. (1984). Strain-rate sensitivity of zinc sheet. *Metallurgical and Materials Transactions A*, *15*(6), 1265-1271.

[82] Molinari, A., Ahzi, S., & Kouddane, R. (1997). On the self-consistent modeling of elastic-plastic behavior of polycrystals. Mechanics of Materials, 26(1), 43-62.

[83] Mercier, S., & Molinari, A. (2009). Homogenization of elastic–viscoplastic heterogeneous materials: Self-consistent and Mori-Tanaka schemes. *International Journal of Plasticity*, 25(6), 1024-1048.

[84] Wang, H., Wu, P. D., Tomé, C. N., & Huang, Y. (2010). A finite strain elastic–viscoplastic self-consistent model for polycrystalline materials. *Journal of the Mechanics and Physics of Solids*, 58(4), 594-612.

[85] Calhoun, C. (2016). Thermomechanical Response of Polycrystalline alpha-Uranium. University of Virginia, PhD Thesis.

[86] Bhattacharyya, J. J., Sasaki, T. T., Nakata, T., Hono, K., Kamado, S., & Agnew, S. R. (2019). Determining the strength of GP zones in Mg alloy AXM10304, both parallel and perpendicular to the zone. *Acta Materialia*, 171, 231-239.

[87] Guo, X. Q., Chapuis, A., Wu, P. D., & Agnew, S. R. (2015). On twinning and anisotropy in rolled Mg alloy AZ31 under uniaxial compression. *International Journal of Solids and Structures*, *64*, 42-50.

[88] Qiao, H., Agnew, S. R., & Wu, P. D. (2015). Modeling twinning and detwinning behavior of Mg alloy ZK60A during monotonic and cyclic loading. *International Journal of Plasticity*, *65*, 61-84.

[89] Wang, H., Clausen, B., Capolungo, L., Beyerlein, I. J., Wang, J., & Tome, C. N. (2016). Stress and strain relaxation in magnesium AZ31 rolled plate: In-situ neutron

measurement and elastic viscoplastic polycrystal modeling. *International Journal of Plasticity*, *79*, 275-292.

[90] Wang, H., Wu, P., Kurukuri, S., Worswick, M. J., Peng, Y., Tang, D., & Li, D. (2018). Strain rate sensitivities of deformation mechanisms in magnesium alloys. *International Journal of Plasticity*, *107*, 207-222.

[91] Nakata, T., Bhattacharyya, J. J., Agnew, S. R., & Kamado, S. (2019). Unexpected influence of prismatic plate-shaped precipitates on strengths and yield anisotropy in an extruded Mg-0.3 Ca-1.0 In-0.1 Al-0.2 Mn (at.%) alloy. *Scripta Materialia*, *169*, 70-75.

[92] Bhattacharyya, J. J., Kada, S. R., Barnett, M. R., & Agnew, S. R. (2019). Crystal plasticity and in-situ diffraction-based determination of the dislocation strengthening and load-sharing effects of precipitates in Mg alloy, AZ91. *Materialia*, *6*, 100308.

[93] Bhattacharyya, J. J., Wang, F., Stanford, N., & Agnew, S. R. (2018). Slip mode dependency of dislocation shearing and looping of precipitates in Mg alloy WE43. *Acta Materialia*, *146*, 55-62.

[94] Bhattacharyya, J. J., Wang, F., Wu, P. D., Whittington, W. R., El Kadiri, H., & Agnew, S. R. (2016). Demonstration of alloying, thermal activation, and latent hardening effects on quasi-static and dynamic polycrystal plasticity of Mg alloy, WE43-T5, plate. *International Journal of Plasticity*, *81*, 123-151.

[95] Armstrong, R. W., Codd, I., Douthwaite, R. M., & Petch, N. J. (1962). The plastic deformation of polycrystalline aggregates. *The Philosophical Magazine: A Journal of Theoretical Experimental and Applied Physics*, *7*(73), 45-58.

[96] Armstrong, R. W. (1968). Theory of the tensile ductile-brittle behavior of poly-crystalline hcp materials, with application to beryllium. *Acta Metallurgica, 16*(3), 347-355.

[97] Yang, K. V., Caceres, C. H., Nagasekhar, A. V., & Easton, M. A. (2012). Low-strain plasticity in a high pressure die cast Mg–Al alloy. *Modelling and Simulation in Materials Science and Engineering*, *20*(2), 024010.

[98] Yakubtsov, I. A., Diak, B. J., Sager, C. A., Bhattacharya, B., MacDonald, W. D., & Niewczas, M. (2008). Effects of heat treatment on microstructure and tensile deformation of Mg AZ80 alloy at room temperature. *Materials Science and Engineering: A*, *496*(1-2), 247-255.

[99] Shabana, M. A., Bhattacharyya, J. J., Niewczas, M., & Agnew, S. R. (2021). Thermally Activated Nature of Basal and Prismatic Slip in Mg and Its Alloys. In *Magnesium Technology 2021* (pp. 53-60). Springer, Cham.

[100] Agnew, S. R., & Duygulu, Ö. (2005). Plastic anisotropy and the role of non-basal slip in magnesium alloy AZ31B. *International Journal of plasticity*, *21*(6), 1161-1193.

[101] Kang, Y. B., Pelton, A. D., Chartrand, P., & Fuerst, C. D. (2008). Critical evaluation and thermodynamic optimization of the Al–Ce, Al–Y, Al–Sc and Mg–Sc binary systems. *Calphad*, *32*(2), 413-422.

[102] Kocks, U. F. (1979). Superposition of alloy hardening, strain hardening, and dynamic recovery. In *Strength of metals and alloys* (pp. 1661-1680). Pergamon.

[103] Conrad, H., & Robertson, W. D. (1957). Effect of temperature on the flow stress and strain-hardening coefficient of magnesium single crystals. *JOM*, *9*(4), 503-512.

[104] Conrad, H., Hays, L., Schoeck, G., & Wiedersich, H. (1961). On the rate-controlling mechanism for plastic flow of Mg crystals at low temperatures. *Acta Metallurgica*, *9*(4), 367-378.

[105] Urakami, A., Meshii, M., & Fine, M. E. (1970). Effect of Li on mechanical properties of Mg base single crystals in basal and prismatic slip.

[106] Sato, A., & Meshii, M. (1973). Solid solution softening and solid solution hardening. *Acta Metallurgica*, *21*(6), 753-768.

[107] Ono, N., Nowak, R., & Miura, S. (2004). Effect of deformation temperature on Hall–Petch relationship registered for polycrystalline magnesium. *Materials Letters*, *58*(1-2), 39-43.

[108] Toda-Caraballo, I., Galindo-Nava, E. I., & Rivera-Díaz-del-Castillo, P. E. (2014). Understanding the factors influencing yield strength on Mg alloys. *Acta Materialia*, *75*, 287-296.

[109] Picu, R. C., Li, R., & Xu, Z. (2009). Strain rate sensitivity of thermally activated dislocation motion across fields of obstacles of different kind. *Materials Science and Engineering: A*, *502*(1-2), 164-171.

[110] Dong, Y., & Curtin, W. A. (2012). Thermally activated plastic flow in the presence of multiple obstacle types. *Modelling and Simulation in Materials Science and Engineering*, *20*(7), 075006.

[111] Picu, R. C. (2004). A mechanism for the negative strain-rate sensitivity of dilute solid solutions. *Acta Materialia*, 52(12), 3447-3458.

[112] Chen, Q., Liu, X. Y., & Biner, S. B. (2008). Solute and dislocation junction interactions. *Acta Materialia*, 56(13), 2937-2947.

[113] DeWit, G., & Koehler, J. S. (1959). Interaction of dislocations with an applied stress in anisotropic crystals. *Physical Review*, *116*(5), 1113.

[114] Schoeck, G., & Frydman, R. (1972). The contribution of the dislocation forest to the flow stress. *Physica status solidi (b)*, 53(2), 661-673.

[115] Kubin, L. P., & Estrin, Y. (1990). Evolution of dislocation densities and the critical conditions for the Portevin-Le Chatelier effect. *Acta metallurgica et materialia*, *38*(5), 697-708.